Influence of nozzle random side loads on launch vehicle dynamics

Nilabh Srivastava, Peter T. Tkacik, and Russell G. Keanini[a)]
Department of Mechanical Engineering, The University of North Carolina at Charlotte, Charlotte, North Carolina 28223, USA

(Received 8 March 2010; accepted 21 May 2010; published online xx xx xxxx)

It is well known that the dynamic performance of a rocket or launch vehicle is enhanced when the length of the divergent section of its nozzle is reduced or the nozzle exit area ratio is increased. However, there exists a significant performance trade-off in such rocket nozzle designs due to the presence of random side loads under overexpanded nozzle operating conditions. Flow separation and the associated side-load phenomena have been extensively investigated over the past five decades; however, not much has been reported on the effect of side loads on the attitude dynamics of rocket or launch vehicle. This paper presents a quantitative investigation on the influence of in-nozzle random side loads on the attitude dynamics of a launch vehicle. The attitude dynamics of launch vehicle motion is captured using variable-mass control-volume formulation on a cylindrical rigid sounding rocket model. A novel physics-based stochastic model of nozzle side-load force is developed and embedded in the rigid-body model of rocket. The mathematical model, computational scheme, and results corresponding to side loading scenario are subsequently discussed. The results highlight the influence of in-nozzle random side loads on the roll, pitch, yaw, and translational dynamics of a rigid-body rocket model.
[doi:10.1063/1.3457887]

I. INTRODUCTION

Given the economics of rocket launch and the need for higher and more reliable dynamic performance, modern rockets are typically designed to achieve high thrust to weight ratios. This objective is often met using advanced nozzle design modifications, including use of high nozzle area ratios, reduced divergent section lengths, and optimized nozzle contours (e.g., TOC, TOP, CTP, etc.[1]). Although such nozzle designs theoretically predict higher vacuum performance, there is a significant performance trade-off associated with these rocket nozzles at sea-level operating conditions. It has been frequently reported[1–3] that supersonic flow in such nozzles tends to be overexpanded, which causes it to unsteadily detach/reattach itself to the nozzle wall. This consequently leads to generation of random nozzle side/lateral loads,[4–7] which are often perilous in nature as they could not only catastrophically affect the vibroacoustic response of rocket, but also affect the safety margins associated with the transient or first-stage of its attitude. In large engines, side-load magnitudes can be extremely large; for example, loads on the order of 250 000 pounds were typically observed during low altitude flight of the Apollo Program's Saturn V rockets.[7] Indeed, minimizing and designing to accommodate potentially catastrophic side loading represents an essential, long-standing design task within the rocket design community.

Supersonic flow separation in a rocket nozzle and the associated side-load phenomena have been extensively investigated both computationally and experimentally over the past five decades. It is well-known[1,8,9] that during overexpanded supersonic nozzle flow conditions, i.e., when P_e (nozzle exit pressure) $< P_a$ (altitude-dependent atmospheric pressure), flow separation involving complex, three-dimensional, and mostly unsteady shock wave boundary layer interactions (i.e., SWBLIs) occurs to compensate for the adverse pressure gradient in the flow direction. This consequently generates large randomly fluctuating lateral forces on the nozzle structure. Turbulent SWBLI remains an extensively studied problem, both theoretically/computationally and experimentally (refer to Chapman *et al.*,[10] Zukoski,[11] Dolling and Murphy,[12] Sinha *et al.*,[13] Polivanov,[14] etc.), AQ: #1 where investigations where performed to study SWBLIs in supersonic flows under the presence of geometrical nonlinearity or discontinuity (e.g., presence of a ramp, step, etc. in flow field), capture unsteady interactions and its affect on instantaneous pressure fluctuations, and predict/analyze separation zone geometry for various flow and wall cooling patterns. With regard to flow separation and side loads in rocket nozzles, Östlund *et al.*[1,4] provide comprehensive reviews of the state of the art, and emphasize the importance of three distinct side-load generation mechanisms: (a) random pressure variations due to free shock separation (FSS), (b) shock transitions, i.e., FSS↔RSS (restricted shock separation, where the separated boundary layer reattaches itself downstream of the separation point to form a recirculation zone), and (c) aeroelasticity, which further amplifies the side loads due to closed-loop fluid-structural vibroacoustic response. Original work on these features has been reported, e.g., by Onofri and Nasuti,[15] Shimizu *et al.*,[16] Frey and Hagemann,[17,18] Pekkari,[19] and Schwane and Xia.[20] AQ: #2

Although work on rocket dynamics and control constitute vast, long studied areas of research (see, e.g., Refs. 21–27), the important question of attitude/ascent dynamics of rockets subject to in-nozzle side loads, surprisingly, remains open. Likewise, vibration control and stability of

a)Electronic mail: rkeanini@uncc.edu.

launch vehicles subject to side loading remains poorly served. It is clear that the development of such control-oriented rocket dynamics models entails an embedding of a fairly accurate description of side-load generation phenomenon, which is a challenging task given the dependence of side loads on a variety of inter-dependent interactions such as internal and external flow patterns, nozzle geometry, ambient conditions, fluid-structure interaction, etc. Although detailed CFD modeling approaches[16,20] have been investigated to yield reasonably accurate predictions of separation point, wall pressure distribution, and nozzle side loads, such models, being computationally intensive, render the synthesis of fast and reliable controllers difficult. Thus, significant research opportunities exist for development of accurate finite-dimensional system-level models suitable for studying the effects of random side loads on rocket attitude dynamics, as well as investigation of the influence of side loads on the stability and elastic and rigid-body response of rockets as they move along their launch trajectory.

The present study has two objectives. First, a simple, yet realistic model of rocket dynamics is sought which takes into account the effects of stochastic, altitude-dependent, in-nozzle side loads. The model will be used to study the influence of these loads on rocket center-of-mass dynamics, stability, and flight trajectory. Given the simplicity of the model, it is anticipated that it could provide a basis for development of, e.g., robust trajectory control strategies and/or structural vibration suppression techniques, particularly during low altitude flight when side loading can be significant.

The second objective of this work centers on development of a simple, physically realistic model of random side-load generation (especially under FSS regime) and evolution during over-expanded low altitude flight. It is clear that knowledge of reasonably accurate separation location and separation criteria will facilitate the development of these physics-based side-load prediction models. A number of criteria[1,3,28,29] have been proposed in past for predicting the nominal FSS point. The side-load prediction model presented in this work is an extended modification of Keanini and Brown,[29] where simple, yet physics-based, scale analyses of transverse momentum transport across the separating boundary layer have been used to derive separation criteria for time-average turbulent SWBL pressure fluctuations in over-expanded nozzles operating under FSS regime. The proposed model focuses on the random shape and motion of the instantaneous in-nozzle boundary layer separation line, and in contrast to existing statistically-based models, requires relatively little experimental or numerical data on the separation-zone wall pressure distribution.

In brief overview, the paper first presents the rocket dynamics model. The proposed model uses a control volume approach, accounts for six degrees of coupled rigid body translational and rotational motion, incorporates a simple, altitude-dependent model of external aerodynamic loading, and accounts for in-nozzle side loads. The model for random, altitude-dependent side loads is then described. Here, a scaling argument is presented indicating that random, spatially varying nozzle-wall pressure distributions immediately up- and down-stream of the instantaneous, azimuthally-varying boundary layer separation line are small relative to the comparatively large, altitude-dependent, mean downstream pressure. This result in turn allows straightforward calculation of the instantaneous side load, given an instantaneous realization of the random separation line shape. It is shown that the model provides straightforward, analytical explanations for several well known side-load statistical properties.

The rocket dynamics model is then used to study the stochastic response of sounding-rocket-scale launch vehicles subject to low altitude random side loads. Although side loads appear only during the earliest portion of flight, their influence on subsequent evolution of pitch, yaw, and lateral displacement is significant; individual realizations of random rocket motion are thus described, as well as ensemble averaged translational and rotational rocket dynamics. Finally, the paper closes with suggestions for future work.

II. ATTITUDE DYNAMICS MODEL OF A RIGID ROCKET

Since the primary objective of this research is to study the influence of nozzle side loads on rocket launch dynamics, a canonical rigid-body rocket model is considered, where the variable-mass and flow dynamics are captured in a comprehensive manner using control volume formulation. Figure 1 illustrates the geometrical description of rocket model along with the forces acting on it. The rocket is subjected to a deterministic, time-dependent aerodynamic load, a time-varying deterministic thrust load, and a stochastic in-nozzle side load. The following assumptions are made during the course of model development.

- Rocket body is axisymmetric at all times.
- The internal flow of burnt products is axisymmetric and steady.
- The instantaneous mass center lies on the longitudinal axis (i.e., the axis of symmetry) at all times and does not undergo significant variation from its initial configuration.
- The line of action of aerodynamic load is along the longitudinal axis of symmetry, i.e., ignore the effects of variable angle of attack (since the primary focus is to investigate the effects of nozzle side loads on rocket dynamics).
- Neglect the effects of stochastic wind loads on rocket dynamics.
- The exhaust gas flow is axisymmetric, uniform, and steady.

Using Reynolds transport theorem and Newton–Euler's momentum equation for a control volume accelerating in a non-inertial frame of reference, one gets

$$\vec{F}_S + \vec{F}_B = \frac{\partial}{\partial t}\int_{CV} \vec{v}\rho dV + \int_{CS} \vec{v}\rho(\vec{v}\,.\,d\vec{A}) + \int_M [\vec{a}_o + 2(\vec{\omega}\times\vec{v}) + \dot{\vec{\omega}}\times\vec{r} + \vec{\omega}\times(\vec{\omega}\times\vec{r})]dM. \quad (1)$$

Here, $\vec{F}_S$ and $\vec{F}_B$ denote all the surface and body forces acting on the control volume of the rocket. ρ, $\vec{v}$, and $\vec{r}$, respectively,

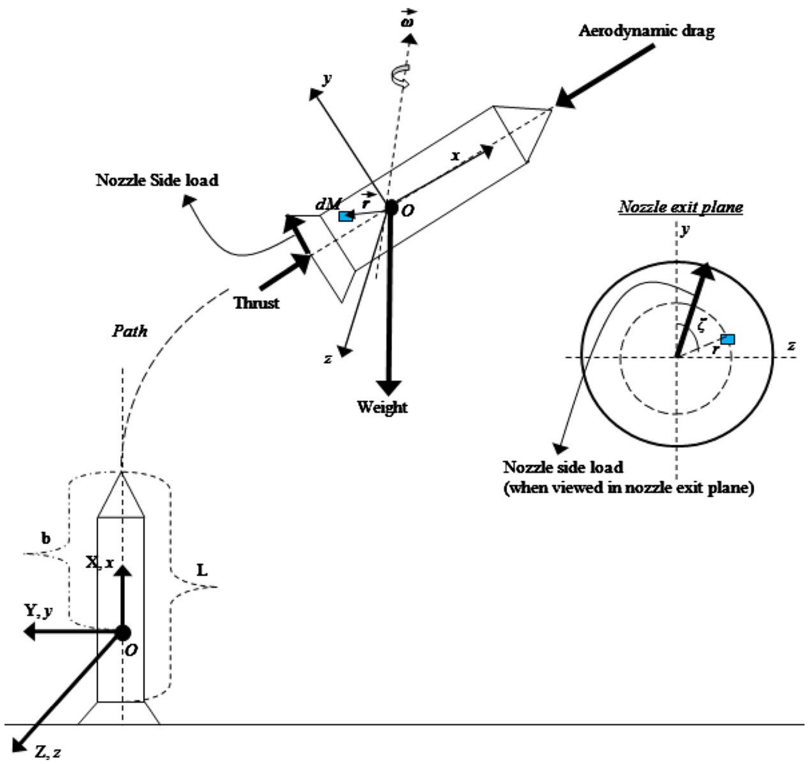

FIG. 1. (Color online) Geometrical description of rigid-body rocket model.

denote the instantaneous density, velocity, and position fields (relative to the control volume) for the flow of combustion products. $\vec{r}$ specifically denotes the distance of an infinitesimal fluid particle from the instantaneous center of mass O, whereas, $\vec{\omega}$ denotes the instantaneous angular velocity of the body-fixed coordinate axes attached to the rocket at its center of mass O. $\vec{a}_o$ denotes the acceleration of the center of mass O of the rocket with respect to an inertial frame of reference (i.e., XYZ in Fig. 1). Given O as the instantaneous center of mass of rocket (i.e., $\int_M \vec{r} dM = 0$) where the body-fixed reference frame is attached and the assumption of steady internal flow of burnt products [i.e., $\partial(\bullet)/\partial t \approx 0$], Eq. (1) could be further simplified as

AQ: #6

$$\vec{F}_S + \vec{F}_B - \int_{CS} \vec{v}\rho(\vec{v} \,.\, d\vec{A}) - \int_M 2(\vec{\omega} \times \vec{v}) dM = M\vec{a}_o. \quad (2)$$

The surface and body forces acting on the rocket can be readily expressed as

$$\vec{F}_S = \vec{F}_A + (p_e - p_a)A_e\vec{i} + F_{sy}\vec{j} + F_{sz}\vec{k},$$

$$\vec{F}_B = -Mg\vec{I}. \quad (3)$$

Here $(\vec{I}, \vec{J}, \vec{K})$ represent the unit vectors of the inertial coordinate axes "XYZ," while $(\vec{i}, \vec{j}, \vec{k})$ represent unit vectors of the body-fixed coordinate axes "*xyz*" with origin at O (the rocket's instantaneous center of mass), as depicted in Fig. 1. Also, p_e is the gas pressure at nozzle exit plane and p_a is the ambient pressure. Recognizing the need to emphasize the dynamic influence of in-nozzle stochastic side loads F_{sy} and F_{sz}, we seek a simple though qualitatively reasonable model of the instantaneous aerodynamic load $(\vec{F}_A)$ as

$$\vec{F}_A = -\frac{1}{2} C_D \rho_a (\dot{x}_o^2 + \dot{y}_o^2 + \dot{z}_o^2) A_R \vec{i}. \quad (4)$$

Thus, the aerodynamic load on the rocket is primarily approximated as a drag force with its line of action coinciding with the longitudinal axis of symmetry (or the x-axis of the body-fixed coordinate frame). Although precise or detailed effects of the angle of attack are not captured by the above-mentioned aerodynamic load model, the Mach number-dependent drag-coefficient C_D [refer to Fig. 2 (Ref. 30)] and the instantaneous changes in the center of mass velocity may serve as useful indicators for analyzing the effects corresponding to variable angle of attack.

Using the mass conservation principle, it is easy to obtain the rate at which mass is being depleted from the rocket control volume

$$\frac{dM}{dt} = -\int_{CS} (\vec{v} \,.\, d\vec{A}). \quad (5)$$

Since the rocket loses mass only through the nozzle exit area (A_e), Eq. (5) could be written as

$$\frac{dM}{dt} = -\int_{A_e} \rho(\vec{v} \,.\, d\vec{A}). \quad (6)$$

Using the assumption of steady axisymmetric exhaust flow and the axisymmetry of rocket nozzle, Eq. (6) yields an expression for the rate of mass loss from the rocket

$$\dot{M} = -\rho_e |v_{ex}| A_e. \quad (7)$$

The above expression for mass loss rate encapsulates the assumption that the density of exhaust gas (ρ_e) does not change appreciably over the nozzle exit plane. v_{ex} is the magnitude of exhaust gas velocity relative to rocket body

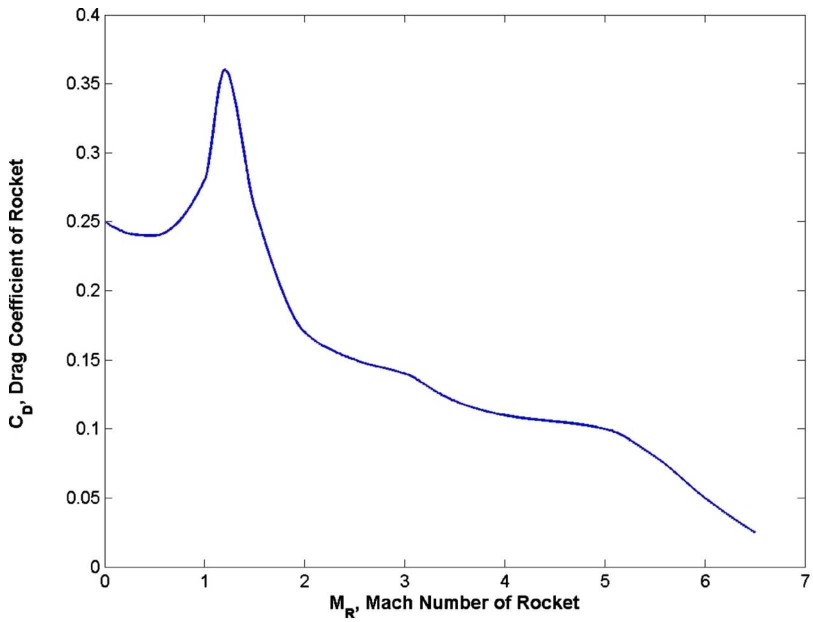

FIG. 2. (Color online) A typical representation of drag coefficient (C_D) vs Mach number for a rocket (Ref. 30).

computed at the nozzle exit plane along the x-direction (i.e., the longitudinal axis of the rocket) of the body-fixed reference frame. Note $\dot{M}$ is constant if the flow through nozzle throat is choked. Using Eqs. (3), (4), and (7), Eq. (2) could be modified to get

$$-\frac{1}{2}C_D\rho_a(\dot{x}_o^2+\dot{y}_o^2+\dot{z}_o^2)A_R\vec{i}+(p_e-p_a)A_e\vec{i}+F_{sy}\vec{j}+F_{sz}\vec{k}-Mg\vec{I} + |\dot{M}|v_{ex}\vec{i}-2\vec{\omega}\int_M \vec{v}dM = M(\ddot{x}_o\vec{I}+\ddot{y}_o\vec{J}+\ddot{z}_o\vec{K}). \quad (8)$$

Using Reynolds transport theorem, the Coriolis term in Eq. (8) could be expanded to obtain

$$-\frac{1}{2}C_D\rho_a(\dot{x}_o^2+\dot{y}_o^2+\dot{z}_o^2)A_R\vec{i}+(p_e-p_a)A_e\vec{i}+F_{sy}\vec{j}+F_{sz}\vec{k}-Mg\vec{I} + |\dot{M}|v_{ex}\vec{i}-2\vec{\omega}\left[\frac{\partial}{\partial t}\int_{CV}\rho\vec{r}dV+\int_{CS}\rho\vec{r}(\vec{v}\,.\,d\vec{A})\right]=M(\ddot{x}_o\vec{I} + \ddot{y}_o\vec{J}+\ddot{z}_o\vec{K}). \quad (9)$$

Again, under the assumption of steady internal flow and negligible variations in center of mass from its initial configuration, Eq. (9) reduces to the following form:

$$-\frac{1}{2}C_D\rho_a(\dot{x}_o^2+\dot{y}_o^2+\dot{z}_o^2)A_R\vec{i}+(p_e-p_a)A_e\vec{i}+F_{sy}\vec{j}+F_{sz}\vec{k} - Mg\vec{I}+|\dot{M}|v_{ex}\vec{i}-2\vec{\omega}[-|\dot{M}|(L-b)\vec{i}]=M(\ddot{x}_o\vec{I}+\ddot{y}_o\vec{J} + \ddot{z}_o\vec{K}). \quad (10)$$

Expressing the angular velocity $\vec{\omega}$ in body-fixed coordinate frame as $\vec{\omega}=\omega_x\vec{i}+\omega_y\vec{j}+\omega_z\vec{k}$ and introducing the Eulerian roll (φ)—pitch (θ)—yaw (ψ) transformation from $(\vec{i},\vec{j},\vec{k})$ reference frame to the inertial $(\vec{I},\vec{J},\vec{K})$ frame

$$\begin{Bmatrix}\vec{i}\\ \vec{j}\\ \vec{k}\end{Bmatrix}=\begin{bmatrix}\cos\psi & \sin\psi & 0\\ -\sin\psi & \cos\psi & 0\\ 0 & 0 & 1\end{bmatrix}\begin{bmatrix}\cos\theta & 0 & -\sin\theta\\ 0 & 1 & 0\\ \sin\theta & 0 & \cos\theta\end{bmatrix} \times\begin{bmatrix}1 & 0 & 0\\ 0 & \cos\varphi & \sin\varphi\\ 0 & -\sin\varphi & \cos\varphi\end{bmatrix}\begin{Bmatrix}\vec{I}\\ \vec{J}\\ \vec{K}\end{Bmatrix}, \quad (11)$$

the following three scalar governing equations for center-of-mass dynamics of rocket could be obtained:

X-motion

$$M\ddot{x}_o=[(p_e-p_a)A_e+|\dot{M}|v_{ex}-0.5C_DA_R\rho_a(\dot{x}_o^2+\dot{y}_o^2 + \dot{z}_o^2)]\cos\theta\cos\psi-Mg-[F_{sy}+2|\dot{M}|(L - b)\omega_z]\cos\theta\sin\psi+[F_{sz}-2|\dot{M}|(L-b)\omega_y]\sin\theta, \quad (12)$$

Y-motion

$$M\ddot{y}_o=[(p_e-p_a)A_e+|\dot{M}|v_{ex}-0.5C_DA_R\rho_a(\dot{x}_o^2+\dot{y}_o^2+\dot{z}_o^2)] \times(\cos\varphi\sin\psi+\sin\varphi\sin\theta\cos\psi)+[F_{sy}+2|\dot{M}| \times(L-b)\omega_z](-\sin\varphi\sin\theta\sin\psi+\cos\varphi\cos\psi) -[F_{sz}-2|\dot{M}|(L-b)\omega_y]\sin\varphi\cos\theta, \quad (13)$$

Z-motion

$$M\ddot{z}_o=[(p_e-p_a)A_e+|\dot{M}|v_{ex}-0.5C_DA_R\rho_a(\dot{x}_o^2+\dot{y}_o^2+\dot{z}_o^2)] \times(\sin\varphi\sin\psi-\cos\varphi\sin\theta\cos\psi)+[F_{sy}+2|\dot{M}| \times(L-b)\omega_z](\cos\varphi\sin\theta\sin\psi+\sin\varphi\cos\psi) +[F_{sz}-2|\dot{M}|(L-b)\omega_y]\cos\varphi\cos\theta. \quad (14)$$

It is evident from Eqs. (12)–(14) that in-nozzle stochastic side loads could significantly influence the translational dynamics of a rocket during its attitude. Also, it is to be noted that the Euler angles (φ,θ,ψ) in these equations timevaryingly depend on the angular velocity $\vec{\omega}$, which further highlights the coupling between the translational and rotational (i.e., roll, pitch, yaw) motions of rocket during its attitude. Using the rotation matrices, one could readily obtain the following relationship between the components of angular velocity in body-fixed reference frame and the time rate of change in Euler angles

$$\begin{Bmatrix}\omega_x\\ \omega_y\\ \omega_z\end{Bmatrix} = \begin{bmatrix}\cos\psi & \sin\psi & 0\\ -\sin\psi & \cos\psi & 0\\ 0 & 0 & 1\end{bmatrix}\begin{bmatrix}\cos\theta & 0 & -\sin\theta\\ 0 & 1 & 0\\ \sin\theta & 0 & \cos\theta\end{bmatrix}\begin{Bmatrix}\dot{\varphi}\\ 0\\ 0\end{Bmatrix}$$

$$+\begin{bmatrix}\cos\psi & \sin\psi & 0\\ -\sin\psi & \cos\psi & 0\\ 0 & 0 & 1\end{bmatrix}\begin{Bmatrix}0\\ \dot{\theta}\\ 0\end{Bmatrix} + \begin{Bmatrix}0\\ 0\\ \dot{\psi}\end{Bmatrix}$$

$$\text{or}\quad \begin{Bmatrix}\omega_x\\ \omega_y\\ \omega_z\end{Bmatrix} = \begin{bmatrix}\cos\theta\cos\psi & \sin\psi & 0\\ -\cos\theta\sin\psi & \cos\psi & 0\\ \sin\theta & 0 & 1\end{bmatrix}\begin{Bmatrix}\dot{\varphi}\\ \dot{\theta}\\ \dot{\psi}\end{Bmatrix}. \qquad (15)$$

It is clear from Eq. (15) that a unique correspondence exists between the time rate of change in Euler angles and the components of angular velocity as long as the above transformation matrix is nonsingular (i.e., unless $\theta = \pm\pi/2$). For the instant when $\theta = \pm\pi/2$, the time rates of Euler angles are obtained using the following equations:

$$\dot{\theta} = \sqrt{\omega_x^2 + \omega_y^2},$$

$$\dot{\psi} = \frac{\omega_y\dot{\omega}_x - \omega_x\dot{\omega}_y}{\omega_x^2 + \omega_y^2},$$

$$\dot{\varphi} = (\omega_z - \dot{\psi})\,\mathrm{sgn}(\sin\theta), \qquad \theta \in \left\{-\frac{\pi}{2}, \frac{\pi}{2}\right\}. \qquad (16)$$

Using generalized Kane's equations, Eke *et al.*[27,31] derived the following vector equation for the rigid-body rotational dynamics of a variable mass system.

$$\bar{\bar{I}}\dot{\vec{\omega}} + \vec{\omega}\times(\bar{\bar{I}}\vec{\omega}) + \frac{d\bar{\bar{I}}}{dt}\vec{\omega} + \int_{\mathrm{CS}}\rho[\vec{r}\times(\vec{\omega}\times\vec{r})](\vec{v}\,.\,d\vec{A})$$

$$+\frac{\partial}{\partial t}\int_{\mathrm{CV}}\rho(\vec{r}\times\vec{v})dV + \int_{\mathrm{CV}}\rho[\vec{\omega}\times(\vec{r}\times\vec{v})]dV$$

$$+\int_{\mathrm{CS}}\rho(\vec{r}\times\vec{v})(\vec{v}\,.\,d\vec{A}) = \vec{M}_{ext}. \qquad (17)$$

Here, $\bar{\bar{I}}$ denotes the principal inertia tensor about the body-fixed axes (xyz), which are also the principal axes. Using the axisymmetry of rocket body, it is assumed $I_{yy} = I_{zz} = I$. The computation of the surface and volume integral terms in Eq. (17) could be readily done as explained subsequently.

The position vector (as shown in Fig. 1) from the instantaneous mass center O to a generic fluid particle leaving nozzle exit area (A_e) could be expressed as

$$\vec{r}|_{A_e} = -(L-b)\vec{i} + r\cos\zeta\vec{j} + r\sin\zeta\vec{k}.$$

The infinitesimal fluid area element at nozzle exit could be expressed as $d\vec{A} = -rdrd\zeta\vec{i}$. The exhaust gas velocity profile (relative to rocket body) over the nozzle exit plane (A_e) is considered to be[31]

$$\vec{v}|_{A_e} = -v_{ex}\vec{i} + \left(\frac{\omega_x r^2}{R_e} - \omega_x r\right)(-\vec{j}\sin\zeta + \vec{k}\cos\zeta). \qquad (18)$$

The $\vec{j}$ and $\vec{k}$ components in the above expression (similar to those introduced by Tran and Eke[31]) account for the effects due to whirling of fluid particles as the rocket (primarily assumed to be a cylindrical body) spins or rolls about its longitudinal axis (i.e., the x-axis of the body-fixed reference frame). The term $\omega_x r^2/R_e$ assumes parabolic distribution of azimuthal velocity field as the fluid particles escape/cross the nozzle exit plane. This is a simplified approximation that accounts for the fact that the fluid particles on the longitudinal axis of symmetry (i.e., x-axis) do not whirl, while those particles at the nozzle surface will whirl with a tangential/peripheral azimuthal velocity of $\omega_x R_e$. Note v_{ex} is not a function of ζ, owing to axisymmetry, and is also assumed to be uniform/constant over the nozzle exit plane. Also, density ρ; is assumed to be uniform over the nozzle exit plane. Using these expressions, the surface integral terms in Eq. (17) could be readily evaluated to yield the following expressions:

$$\int_{\mathrm{CS}=A_e}\rho(\vec{r}\times\vec{v})(\vec{v}\,.\,d\vec{A}) = -\frac{|\dot{M}|}{10}\omega_x R_e^2\vec{i}. \qquad (19)$$

$$\int_{\mathrm{CS}=A_e}\rho[\vec{r}\times(\vec{\omega}\times\vec{r})](\vec{v}\,.\,d\vec{A}) = |\dot{M}|\{((L-b)^2 + 0.25R_e^2)$$

$$\times(\omega_y\vec{j} + \omega_z\vec{k}) + 0.5R_e^2\omega_x\vec{i}\}. \qquad (20)$$

For the volume integral term [i.e., the sixth term in Eq. (17)], the contributions from geometrical nonuniformities in rocket body and nozzle sections are neglected and the rocket combustion chamber is primarily treated as a cylinder of radius R_i with an axisymmetric internal flow field having a velocity profile (relative to rocket body) similar to Eq. (18) (Ref. 31)

$$\vec{v} = -v_x\vec{i} + \left(\frac{r}{R_i} - 1\right)\omega_x r(-\vec{j}\sin\zeta + \vec{k}\cos\zeta); \quad v_x \neq f(\zeta). \qquad (21)$$

The position vector from the instantaneous mass center O to a generic fluid particle contained within the rocket body is given by $\vec{r} = \hat{x}\vec{i} + r\cos\zeta\vec{j} + r\sin\zeta\vec{k}$. The infinitesimal fluid volume element could be expressed as $dV = rdrd\zeta d\hat{x}$. Using these expressions, the volume integral term [i.e., the sixth term in Eq. (17)] could be evaluated to yield the following expression:

AQ: #8

$$\int_{CV} \rho[\vec{\omega} \times (\vec{r} \times \vec{v})]dV = -\frac{|\dot{M}|LR_i^4}{10v_{ex}R_e^2}(\omega_x\omega_z\vec{j} - \omega_x\omega_y\vec{k}). \tag{22}$$

It is clear that this volume integral term in fact captures the gyroscopic torques that the rocket experiences during its attitude. Using Eqs. (19), (20), and (22) and the assumption of steady internal flow, Eq. (17) could be simplified to yield the following three governing equations for the rotational dynamics of rocket during its attitude:

$$I_{xx}\dot{\omega}_x + \left(\dot{I}_{xx} + \frac{2}{5}|\dot{M}|R_e^2\right)\omega_x = 0, \tag{23}$$

$$I\dot{\omega}_y + (I_{xx} - I)\omega_x\omega_z + \dot{I}\omega_y + |\dot{M}|[(L-b)^2 + 0.25R_e^2]\omega_y - \frac{|\dot{M}|LR_i^4}{10v_{ex}R_e^2}\omega_x\omega_z = \vec{M}_{ext}\cdot\vec{j}, \tag{24}$$

$$I\dot{\omega}_z - (I_{xx} - I)\omega_x\omega_y + \dot{I}\omega_z + |\dot{M}|[(L-b)^2 + 0.25R_e^2]\omega_z + \frac{|\dot{M}|LR_i^4}{10v_{ex}R_e^2}\omega_x\omega_y = \vec{M}_{ext}\cdot\vec{k}. \tag{25}$$

Since the line of action of aerodynamic load is assumed to coincide with the longitudinal axis (i.e., x-axis of body-fixed frame) through the center of mass O of the rocket, the only force that contributes to the external moment term $\vec{M}_{ext}$ in Eqs. (24) and (25) is the in-nozzle stochastic side load. The moment due to these stochastic side loads could be computed as

$$\vec{M}_{ext} = -(L-b)\vec{i} \times (F_{sy}\vec{j} + F_{sz}\vec{k}). \tag{26}$$

Thus, Eqs. (12)–(16) and (23)–(26) together constitute the governing equations for translational and rotational dynamics of a variable-mass rigid-rocket during its attitude. It is clear from these equations that the stochastic lateral loads on the nozzle walls could significantly influence the dynamic response of rocket, which could be undesirable or perilous. The subsequent section discusses the mathematical model for computation of these stochastic side loads (i.e., F_{sy} and F_{sz}) on the rocket nozzle.

It is evident from the governing equations of rocket model that a fairly accurate description of altitude-dependent atmospheric pressure and density is needed for capturing the overexpanded flow dynamics. Thus, a National Aeronautics and Space Administration (NASA) atmospheric model is adopted from literature[32] and embedded in the above governing equations. The NASA atmospheric model for ambient pressure, temperature, and density is given by the following equations:

$$p_a(\text{in kPa}) = \begin{cases} 101.29\left(\dfrac{T_a + 273.1}{288.08}\right)^{5.256}, & x_o < 11000 \text{ m(i.e. meters)} \\ 22.56e^{(1.73-0.000157x_o)}, & 11000 \text{ m} < x_o < 25\,000 \text{ m}, \\ 2.488\left(\dfrac{T_a + 273.1}{216.6}\right)^{-11.388}, & x_o > 25\,000 \text{ m} \end{cases}$$

$$T_a(\text{in }^\circ\text{C}) = \begin{cases} 15.04 - 0.006\,49x_o, & x_o < 11\,000 \text{ m} \\ -56.46, & 11\,000 \text{ m} < x_o < 25\,000 \text{ m}, \\ -131.21 + 0.002\,99x_o, & x_o > 25\,000 \text{ m} \end{cases}$$

$$\rho_a(\text{in kg/m}^3) = \frac{p_a}{0.2869(T_a + 273.1)}.$$

III. NOZZLE SIDE-LOAD MODEL FOR FSS REGIME

Broadly speaking, the origin of side loads on rocket nozzles can be traced to one or more of the following features: steady and/or time varying asymmetries in the nozzle flow and pressure fields, steady and/or time-varying asymmetries in nozzle shape, and external aerodynamic loading. Focusing on the first case, the following chain of physical processes can create side loads.

A. Side load physical processes

During low altitude flight, ambient pressure can, and often does, exceed near-exit pressures within the nozzle, i.e., the nozzle flow can be overexpanded. Under these conditions, excess external pressure can force ambient air upstream into the nozzle, where the incoming flow is confined to the low inertia near-wall region. This counter-flow continues upstream to a locus of points, the nominal boundary layer separation line, $s(\phi,t)$ (as depicted in Fig. 3), at which a balance between (decaying) upstream inertia and downstream boundary layer inertia causes separation of the latter.

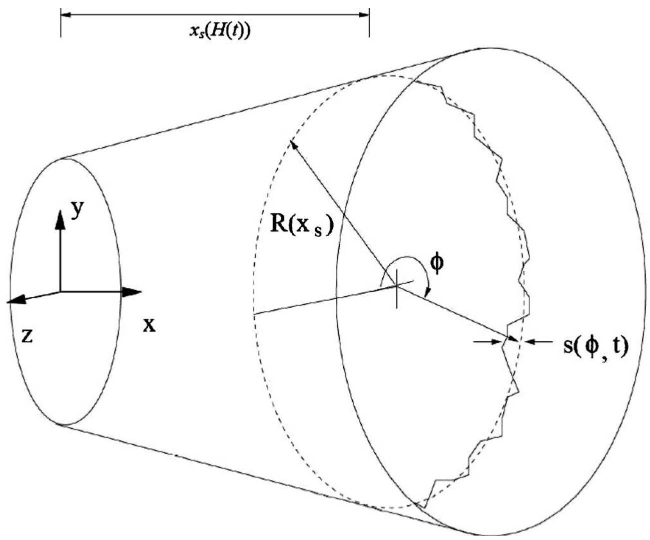

FIG. 3. Schematic of instantaneous boundary layer separation line shape, $s(\phi,t)$. The time, or equivalently, altitude-dependent mean separation line location (along the nozzle's longitudinal axis) is denoted as $x_s[H(t)]$, where $H(t)$ is the instantaneous rocket altitude. The corresponding nozzle radius is $R(x_s)$.

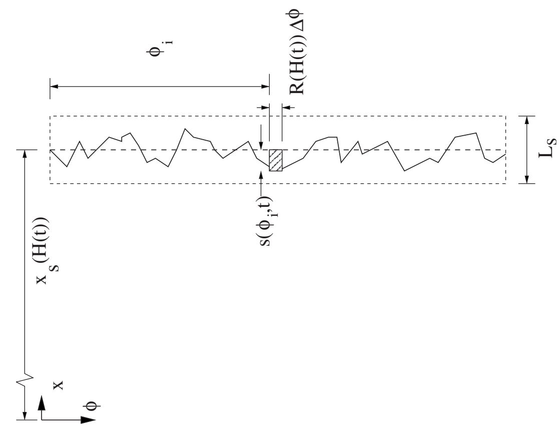

FIG. 4. Separation line model: the mean separation line position, $x_s[H(t)]$, moves down the nozzle axis, x on the slow time scale associated with vertical rocket motion. By contrast, axial separation line motion about $x_s[H(t)]$, at any angular position, ϕ_i, is random, and takes place on a much shorter time scale; rapid axial motion, in addition, is confined to the nominal shock boundary layer interaction zone, denoted by L_s. Pressures upstream (P_i) and downstream (P_2) of the instantaneous separation line, $s(\phi,t)$, are assumed to be spatially uniform within L_s, but do vary with rocket altitude, $H(t)$.

The separating boundary layer, in turn, forms a virtual turning corner along the nozzle wall, triggering formation of a three-dimensional oblique shock structure within the external supersonic, nonboundary layer flow. The shape of $s(\phi,t)$ is random and asymmetric. Thus, due to the pressure jump across the associated oblique shock, a net, nominally-radial pressure force, the side load, $\mathbf{F_r}(t)$ *(boldface font represents vector quantity)*, acts on the nozzle wall. Due to the random, time-varying shape of $s(\phi,t)$, the instantaneous magnitude, $A(t)=|\mathbf{F_r}(t)|=\sqrt{F_{sy}^2+F_{sz}^2}$, and direction, ϕ, of $\mathbf{F_r}$ likewise vary randomly in time. Two distinct shock-boundary layer separation structures, the FSS and RSS structure, appear to play prominent roles in nozzle side loading.[1,4–6] Although the model proposed here applies to side loads associated with the FSS structure, a similar approach can be adapted to side loading associated with RSS structures.

Current side-load models can be characterized as one of two types, phenomenological models which attribute side loading to, e.g., a fixed boundary layer separation line within the nozzle,[33] or, more recently, semiempirical statistical models[4,34,35] which require experimentally measured correlations of the nozzle wall pressure field. Dumnov[34] introduced the latter approach in 1996 and his ideas now dominate this area of research.

The objectives of this section are threefold. First, we wish to propose an alternative probabilistic approach to Dumnov for computing side loads. As described here, the present approach focuses on the statistical behavior of the random separation line, $s(\phi,t)$. Second, closure of existing probabilistic side-load models requires either complex experimental measurements of nozzle wall pressure distributions, or development of high-level compressible flow simulations capable of capturing complex three-dimensional, unsteady shock boundary layer interactions.[1,35,36] We wish to develop a relatively simple, physically consistent model of separation line motion and side loading that circumvents the heavy experimental and numerical modeling demands associated with present approaches. Specifically, we propose a purely analytical solution to the closure problem. Third, while altitude effects play a crucial role in side-load evolution and behavior, this important feature has not been examined. Thus, we incorporate this effect within the proposed model.

The proposed side-load model requires statistical information on two random features: (i) the instantaneous azimuthal pressure distribution in the vicinity of the instantaneous in-nozzle boundary layer separation line, $s(\phi,t)$, and (ii) the instantaneous, azimuthally varying shape of $s(\phi,t)$ (refer to Figs. 3 and 4).

With regard to the first feature, scaling arguments below indicate that at any instant, spatial pressure fluctuations immediately upstream and downstream of the instantaneous separation line are small relative to associated (spatially uniform) mean pressures. At first glance, this appears to contradict the well known observation[34] that pressures near the separation line exhibit significant random variations in both the axial and azimuthal directions. However, based on our scaling analysis, we argue that these observations reflect random fluctuations in the separation line shape, taking place within near-uniform upstream and downstream wall pressure fields.

Comparing experimental requirements necessary for closure of Dumnov's model[34] versus those required for closure of the present model, since Dumnov[34] ignores separation line dynamics, his approach again requires experimentally or numerically generated data on the axially and azimuthally varying nozzle wall pressure distribution (obtained in the vicinity of the boundary layer separation zone). The present approach, by contrast, exploits the well-known observation[37–40] that *local* separation line dynamics exhibit fairly universal statistical characteristics, independent of the shock generator, nozzle type, and separation location. [Here, and with reference to Fig. 4, *local* refers to separation line motion observed within a thin rectangular region of (say) lateral width $R\Delta\phi$ and axial length L_s, where R and L_s are defined below and in the caption.] Presuming that the statistics of separation line motion remain nominally independent of azimuthal position (within circular nozzles), the experimental effort required for closure here thus appears to be significantly less; again, we use simple analytical modeling in order to achieve closure.

B. Probabilistic side-load model

Considering the instantaneous force vector produced by asymmetric boundary layer separation, $\mathbf{F_s}(t)$, expressed as a sum of radial and axial components

$$\mathbf{F_s}(t) = \mathbf{F_r}(t) + \mathbf{F_x}(t), \tag{27}$$

we note the following important experimental and numerical observations concerning the side load, $\mathbf{F_r}$, (within rigid, axisymmetric nozzles):

(a) the probability density of the random amplitude, $A = |\mathbf{F_r}|$, is a Rayleigh distribution[34,35] and
(b) the random instantaneous direction, ϕ, of $\mathbf{F_r}$ is uniformly distributed over the periphery of the nozzle, or $p_\phi(\phi)=1/2\pi$, where p_ϕ is the pdf of the side-load direction.[35]

In this subsection, we adapt a discussion from Ref. 41 to show that both observations can be explained using a simple statistical model of random side loads. Knowing A and ϕ, it is trivial to express the instantaneous side-load components in body-fixed y- and z-directions as $F_{sy}=A\cos\phi$ and $F_{sz}=A\sin\phi$. The following assumptions were made regarding the statistics of F_{sy} and F_{sz}:

(i) F_{sy} and F_{sz} are independent, Gaussian random variables,
(ii) $\langle F_{sy}\rangle=0$ and $\langle F_{sz}\rangle=0$, and
(iii) $\langle (F_{sy}-\langle F_{sy}\rangle)^2\rangle=\langle (F_{sz}-\langle F_{sz}\rangle)^2\rangle=\sigma^2$,

where, assuming ergodicity, $\langle\cdot\rangle$ denotes either an ensemble or time average. As shown in Sec. IV, the first two assumptions can be derived from the model of separation line dynamics presented there and in Sec. III, the last assumption reflects the presumption that the random flow features underlying side loading are azimuthally homogeneous.

AQ: #10

Thus, writing F_{sy} and F_{sz} as, $F_{sy}=\bar{Y}=A\cos\phi$ and $F_{sz}=\bar{Z}=A\sin\phi$, the joint probability density associated with F_{sy} and F_{sz} can be expressed as

$$p_{\bar{Y}\bar{Z}}(\bar{Y},\bar{Z}) = p_{\bar{Y}}(\bar{Y})\cdot p_{\bar{Z}}(\bar{Z}) = \frac{1}{2\pi\sigma^2}\exp\left(-\frac{\bar{Y}^2+\bar{Z}^2}{2\sigma^2}\right). \tag{28}$$

Following Ref. 41, we restate $p_{\bar{Y}\bar{Z}}$ in terms of A and ϕ as,

$$p_{A\phi} = |J|\, p_{\bar{Y}\bar{Z}}(\bar{Y},\bar{Z}), \tag{29}$$

where $p_{A\phi}(A,\phi)$ is the joint pdf for the random amplitude and direction of $\mathbf{F_r}$, and where the Jacobian determinant is given by

$$|J| = \left|\begin{matrix} \dfrac{\partial\bar{Y}}{\partial A} & \dfrac{\partial\bar{Y}}{\partial\phi} \\ \dfrac{\partial\bar{Z}}{\partial A} & \dfrac{\partial\bar{Z}}{\partial\phi}\end{matrix} = A\right|. \tag{30}$$

Thus,

$$p_{A\phi}(A,\phi) = \frac{A}{2\pi\sigma^2}\exp\left(-\frac{A^2}{2\sigma^2}\right) = \left(\frac{1}{2\pi}\right)\left[\frac{A}{\sigma^2}\exp\left(-\frac{A^2}{2\sigma^2}\right)\right]$$
$$= p_\phi(\phi)p_A(A), \tag{31}$$

where

$$p_\phi(\phi) = \frac{1}{2\pi}, \quad 0<\phi\le 2\pi, \tag{32}$$

is again the uniform probability density underlying the random direction ϕ and

$$p_A(A) = \frac{A}{\sigma^2}\exp\left(-\frac{A^2}{2\sigma^2}\right), \tag{33}$$

is the Rayleigh distribution for the amplitude A.

It is thus clear that the simple assumptions (i)–(iii) above provide a basis for explaining and modeling known side-load statistical properties. In addition, this appears to be the first analytical, i.e., nonexperimental and nonnumerical, explanation of the observations[34,35] noted in (a) and (b) above.

C. Model closure: Separation line shape

In order to close the statistical description of random side loads, the parameter σ in Eqs. (31) or (33) must be determined. In this section, we

(i) relate σ to $\langle A^2\rangle$ and
(ii) propose a model of separation line dynamics.

The second task rests on simple scale analyses of the fluid dynamical features extant within, and near, the shock-boundary layer interaction zone, as well as introduction of simple assumptions on the statistics of separation line motion. Given the separation line model, the side-load model can then be closed, as described in Sec. IV.

The parameter σ can be related to $\langle A^2\rangle$ by first noting from the statistical model of the side-load components F_{sy} and F_{sz}, that

$$\langle (F_{sy}-\langle F_{sy}\rangle)^2\rangle = \langle F_{sy}^2\rangle = \sigma^2,$$

$$\langle (F_{sz}-\langle F_{sz}\rangle)^2\rangle = \langle F_{sz}^2\rangle = \sigma^2. \tag{34}$$

Since, $A^2=F_{sy}^2+F_{sz}^2$, we get

$$\langle A^2\rangle = \langle F_{sy}^2\rangle + \langle F_{sz}^2\rangle = \sigma^2+\sigma^2 = 2\sigma^2 \tag{35}$$

or

$$\sigma = \frac{1}{\sqrt{2}}\sqrt{\langle A^2\rangle}. \tag{36}$$

Equation (36) could also have been directly obtained using standard formulae for the Rayleigh distribution[41] $\langle A\rangle = \sigma\sqrt{\pi/2}$, $\mathrm{var}(A)=\sigma^2(4-\pi)/2$, and $\mathrm{var}(A)=\langle A^2\rangle-\langle A\rangle^2$.

1. Model of separation line motion

Considering the random axial (streamwise) motion of the boundary layer separation line, we take advantage of a separation in time scales, τ_R and τ_s, associated, respectively, with the slow downstream motion of the line's mean position, $x_s(t)=x_s(x_o(t)=H(t))$, and the rapid motion of the separation line about $x_s(t)$. The mean position of the separation line moves downstream in response to the decaying external ambient pressure; thus, τ_R is estimated as $\tau_R=\Delta H_a/V_R$, where ΔH_a is the characteristic incremental altitude over which significant ambient pressure changes occur and V_R is a characteristic rocket speed. By contrast, τ_s corresponds to the lower end of the frequency spectrum associated with large amplitude, random axial motion of the separation line about x_s; this lower end ranges from approximately 10 to 300 Hz while the amplitude of random axial motion, delimiting the nominal shock-boundary layer interaction zone, ranges from approximately 1 to 5 cm.[39]

Thus, since $\tau_R \gg \tau_s$, then over time intervals $\Delta t=O(\tau_R)$, well defined statistical features associated with the fast separation line motion about $x_s(t)$ can, at any given instant, be reliably determined. Given this difference in time scales, we propose the following model of separation line motion:

(i) Assume that at any altitude $H=H(t)=x_o(t)$, a stationary, time (or equivalently, ensemble) average separation line shape, $\bar{s}(H)$, exists, where averaging is carried out over intervals T that are long relative to τ_s, but short relative to τ_R.

(ii) Assume that the mean separation line shape, $\bar{s}(H)$, is independent of the azimuthal angle ϕ. This is a reasonable assumption for FSS within nominally symmetric nozzles that are attached to well-designed combustion chambers that do not produce significant asymmetric combustion.

(iii) At any altitude H, or equivalently, any time t, discretize the instantaneous separation line shape into N equiangular increments, $\Delta\phi$. As shown in Fig. 4, we define a circular reference line passing around the inner periphery of the nozzle, where the reference line coincides with the mean axial separation line location, $x_s[H(t)]$. In addition, define N differential areas

$$\Delta A_i = R(x_s(t))s(\phi_i,t)\Delta\phi, \quad i=1,2,\ldots,N, \tag{37}$$

where $R[x_s(t)]$ is the nozzle inner radius at $x_s(t)=x_s[H(t)]$, and $s(\phi_i,t)$ is the instantaneous axial position of the separation line at $\phi=\phi_i$, relative to the (time-varying) reference line.

(iv) Define, at any given altitude H, a shock-boundary layer interaction zone of axial length L_s which encompasses the axial region over which the separation line moves. Assume that within this zone pressures upstream and downstream of the instantaneous separation line, $P_i(t)=P_i\{x_s[H(t)]\}$ and $P_2(t)=P_2[H(t)]$, respectively, are independent of ϕ and only depend on altitude $H=H(t)$.

In order to justify these assumptions, and as an important aside prior to listing the last two model assumptions, we use scaling to argue that spatial pressure variations both up- and downstream of $x_s(t)$, within the nominal shock-boundary layer interaction zone, are small relative to the respective (background, slowly time varying) mean pressures, $P_i(t)$ and $P_2(t)$.

Considering first the upstream side of the instantaneous separation line, three potential sources of spatial pressure variations can be identified: azimuthal acoustic pressure modes within the upstream in viscid supersonic flow, upstream transmission of acoustic disturbances within subsonic portions of the turbulent boundary layer, and dynamic pressure produced by the turbulent boundary layer. Pressure variations produced by azimuthal acoustic modes are likely minimal since these modes cannot propagate (azimuthally) more than a distance of order $O(L_s/M_i)$ (where M_i is the free stream Mach number at the incipient separation point).

With regard to the second source, while Liepmann *et al.*[42] observed that acoustic disturbances travel no more than one or two boundary layer thicknesses upstream within turbulent compressible boundary layers, in relatively thick boundary layers, such disturbances *could* produce spatial pressure variations on the upstream side of the instantaneous separation line. However, extending an argument given immediately below, since the maximum characteristic magnitude of these variations, $\Delta p'$, is small relative to the characteristic pressure *difference*, P_2-P_i across the separation line (where the latter is used to calculate side loads), then even in cases where acoustic disturbances penetrate well upstream of the separation line, for computational purposes, we can neglect the associated pressure variation.

Finally, considering pressure variations due to boundary layer turbulence, the ratio of turbulent pressure variations to the mean pressure is on the order of $p'/\bar{P}_i=O(u'^2/\bar{U}^2)$, where the latter, representing the ratio of characteristic upstream random to mean velocities, is small.

On the downstream side of the instantaneous separation line, a large, *subsonic*, near-wall separation zone exists.[1,4,36] Acoustic pressure fluctuations at and near the nozzle exit, as well as those within the separation zone, can thus propagate upstream, and indeed, these fluctuations are implicated as the primary source of the low frequency, large amplitude separation line motions noted above. [High frequency, small amplitude jitter is also observed[39] and appears to be produced by advection of vorticity through the foot of the separation-inducing shock.] Since spatial pressure variations *upstream* of the instantaneous separation line appear to be small (as argued above), we can use the characteristic magnitude of the random *downstream* pressure fluctuations, $\Delta p'$, as a useful estimate of the *maximum* pressure fluctuations extant within the entire shock-boundary layer interaction zone.

An estimate for $\Delta p'$ follows via two equivalent routes: (i) focus on the axial dynamics of boundary layer particles immediately downstream of the instantaneous separation line and scale particle inertia against the net axial pressure force[29] or (ii) scale axial inertia, $\rho u_t \approx \rho_2 L_s/\tau_s^2$, against pressure, $P_x \approx \Delta p'/L_s$, in the Navier–Stokes equations. Either approach leads to

$$\Delta p'/P_2 \approx \Delta p'/P_a \approx (\rho_a L_s/\tau_s^2)/P_a \ll 1, \tag{38}$$

where the downstream density and pressure, ρ_2 and P_2, are approximately equal to (altitude-dependent) ambient values, ρ_a and P_a. Thus, over the boundary layer-shock interaction zone, spatial pressure variations on either side of the instantaneous separation line are small relative to the instantaneous (altitude dependent) downstream mean, $P_2[H(t)]$ (and again, are thus small relative to $P_2 - P_i$).

(v) Returning to the model, we express the probability of observing any given instantaneous separation line shape, $s(\phi,t)$, as a joint probability density

$$p_s = p_s(s_1, s_2, \ldots, s_N), \tag{39}$$

over the N-dimensional set of random variables describing the shape

$$[s_1 = s(\phi_1,t),\ \ s_2 = s(\phi_2,t),\ \ s_3 = s(\phi_3,t),\ \ldots,\ \ s_N = s(\phi_N,t)]$$

and assume that each member of the set $[s_1, s_2, s_3, \ldots, s_N]$ is

(a)independent,
(b)Gaussian, and
(c)has the same (altitude-dependent) variance, $\mathrm{var}(s_i) = \sigma_s^2 = \sigma_s^2(H)$.

Considering first assumption (a), we expect that under conditions where large downstream azimuthal acoustic modes are not excited (such as those implicated in tee-pee separation patterns,[1,5] for example), this assumption is approximately valid. In addition, this assumption leads to considerable mathematical simplification. Assumption (b) is consistent with earlier observations,[4,43] while (c) appears reasonable, again under conditions where nozzle shape and combustion are nominally symmetric, and where downstream flow asymmetries are small. Taken together, and as shown below, these assumptions lead to theoretical results, given in Eq. (46) below, that are consistent with observed side-load statistical properties.

(vi) Finally, when moving from the discrete to continuous limit, $\Delta\phi \to d\phi$, and consistent with assumptions (va) and (vc) above, we assume that the instantaneous separation line, $s(\phi,t)$, is delta correlated in ϕ

$$\langle s(\phi,t), s(\phi',t)\rangle_s = \sigma_s^2 \delta(\phi - \phi'), \tag{40}$$

where $\langle\cdot\rangle_s$ denotes an ensemble average over the space of all separation line shapes.

D. Side-load statistical properties

Having proposed a statistical model of separation line dynamics, we can now calculate side-load statistical properties, specifically ensemble averages of the lateral side-load components, $\langle F_{sy}\rangle_s$ and $\langle F_{sz}\rangle_s$, and importantly for present purposes, the mean squared side-load amplitude, $\langle A^2\rangle_s$.

Based on assumptions (va)—vc) above, the joint probability density, p_s, associated with the instantaneous random separation line shape is given by

$$p_s(s_1, s_2, \ldots, s_N) = \prod_I p_I = \frac{1}{(2\pi\sigma_s)^{N/2}} \times \exp\left(-\frac{s_1^2 + s_2^2 + \ldots + s_N^2}{2\sigma_s^2}\right). \tag{41}$$

Expressing p_s as the product of the N Gaussian pdfs, p_I, $I = 1, 2, \ldots, N$, where each p_I, given by

$$p_I(s_I) = \frac{1}{\sqrt{2\pi\sigma_s^2}} \exp\left(-\frac{s_I^2}{2\sigma_s^2}\right), \tag{42}$$

is again associated with the independent random line displacement, $s_I = s(\phi_I, t)$.

Ensemble averages of the instantaneous side-load components F_{sy} and F_{sz} then follow as:

$$\langle F_{sy}[H(t)]\rangle_s = R[H(t)]\{P_i[H(t)] - P_a[H(t)]\} \int_0^{2\pi} \sin\phi \langle s(\phi,t)\rangle_s d\phi \tag{43}$$

and

$$\langle F_{sz}[H(t)]\rangle_s = R[H(t)]\{P_i[H(t)] - P_a[H(t)]\} \int_0^{2\pi} \cos\phi \langle s(\phi,t)\rangle_s d\phi, \tag{44}$$

where we approximate the downstream pressure, $P_2[H(t)]$ as the instantaneous ambient pressure, $P_a[H(t)]$.[29,36] In order to evaluate these averages, express the kth realization of, e.g., $F_{sy}^{(k)}$, in discrete form as

$$F_{sy}^{(k)}(s_1, s_2, \ldots, s_N) = R[H(t)]\{P_i[H(t)] - P_a[H(t)]\} \times \sum_{I=1}^{N} s^{(k)}(\phi_I)\sin(\phi_I)\Delta\phi, \tag{45}$$

where $s^{(k)}(\phi_I)$ is the associated separation line displacement at ϕ_I. Taking the ensemble average term by term, and noting that

$$\langle s_I\rangle_s = \int_{-\infty}^{\infty}\int_{\infty}^{\infty}\cdots\int_{-\infty}^{\infty} s_I p_s(s_1, s_2, \ldots, s_N) ds_1 ds_2 \ldots ds_N = 0,$$

then leads to the result that ensemble averaged values of both side-load components are zero

$$\langle F_{sy}[H(t)]\rangle_s = 0, \quad \langle F_{sz}[H(t)]\rangle_s = 0. \tag{46}$$

The altitude-dependent average squared side-load amplitude, $\langle A^2[H(t)]\rangle_s$, is finally determined as follows:

$$A^2[H(t)] = F_{sy}^2(H) + F_{sz}^2(H) = R^2[H(t)]\{P_i[H(t)] - P_a[H(t)]\}^2\left\{\left[\int_0^{2\pi} s(\phi)\cos\,\phi d\phi\right]^2 + \left[\int_0^{2\pi} s(\phi)\sin\,\phi d\phi\right]^2\right\}$$

or

$$A^2[H(t)] = R^2[H(t)]\{P_i[H(t)] - P_a[H(t)]\}^2 \times\left[\int_0^{2\pi}\int_0^{2\pi} s(\phi)s(\phi')\cos(\phi-\phi')d\phi d\phi'\right]. \tag{47}$$

Taking the average $\langle A^2\rangle_s$, and using Eq. (40), we get

$$\langle A^2\rangle = \langle A^2[H(t)]\rangle = 2\pi\sigma_s^2 R^2[H(t)]\{P_i[H(t)] - P_a[H(t)]\}^2. \tag{48}$$

Taking σ_s as the experimentally observed (nominal) length of the shock interaction zone, L_s, the sideload model is closed finally by using the right side of Eq. (48) in Eq. (36), yielding the parameter σ in Eq. (31) [(or Eq. (33)].

IV. RESULTS AND DISCUSSION

The rocket dynamics model used for numerical experiments corresponds to the translational and rotational equations of motion, Eqs. (12)–(14) and (23)–(25). During the side-loading period, $0 \le t < T$, this nonlinear coupled system is forced by random nozzle side loads. In order to simulate any given side-load history, a three-step Monte Carlo approach is employed. First, at any instant t, the instantaneous mean separation line location, $x_s(t)$, is determined using an approach outlined in Keanini and Browm.[29] Thus, an approximate nozzle pressure ratio is first calculated as

$$\mathrm{NPR}(t) = \frac{P_o}{P_a[H(t)]} = \frac{P_o}{P_i}\frac{P_i}{P_2}\frac{P_2}{P_a[H(t)]} = g(M_i)f(M_i,\beta)c(t), \tag{49}$$

where $g(M_i)=P_0/P_i$, $f(M_i,\beta)=P_i/P_2$, $c(t)=P_2/P_a(H(t))$, P_i and P_2 are pressures upstream and downstream of the separation-inducing shock, β is the shock angle, and M_i is the associated upstream Mach number. The implicit function $g(M_i)$ is obtained via the generalized quasi-one-dimensional model of isentropic flow[44] while $f(M_i,\beta)$ corresponds to the pressure ratio function for oblique shocks based on Keanini and Brown separation criteria.[29] The function $c(t)$ captures the small down-stream pressure rise that drives flow within the near-nozzle-wall recirculation zone; generalizing, e.g., the results from Keanini and Brown[29] to the present case of time-varying ambient pressure, we assume that $c(t)=0.85$. Similarly, and consistent with a number of shock angle measurements (see literature overview in Ref. 29), we take the shock/flow deflection angle $\theta \approx 15.2°$. Again, using the well-known shock relationship [see Eq. (50)], the turning/deflection angle θ can be easily expressed (especially for the in viscid flow outside the separating boundary layer) as a function of incipient Mach number M_i and the shock angle β (Ref. 44)

TABLE I. Model simulation parameters and values.

Parameters	Values
Mass of rocket, M (at $t=0$)	1200 kg
Nozzle exit radius, R_e	0.25 m
Nozzle throat radius	0.05 m
Radius of main rocket body, R_i	0.2 m
Nozzle divergent section angle	15°
Length of rocket, L	10 m
Location of center of mass of rocket from the apex, b	5 m
Moment of inertia about roll axis, I_{xx} (at $t=0$)	135 kg m^2
Moment of inertia about yaw/pitch axis, I (at $t=0$)	10 000 kg m^2
Combustion chamber pressure (stagnation pressure), P_0	7 MPa
Combustion chamber temperature (stagnation temperature), T_0	3600 K
Polytropic exponent of exhaust gas	1.34
Gas constant for exhaust gas	355.47 J/kg m^2
Polytropic exponent of ambient air	1.4
Gas constant for ambient air	287 J/kg K

$$\tan\,\theta = \frac{2\cot\,\beta(M_i^2\sin^2\beta - 1)}{M_i^2(\gamma + \cos\,2\beta) + 2}. \tag{50}$$

Thus, given NPR(t) and turning angle θ, Eqs. (49) and (50) allow determination of the associated incipient upstream Mach number, $M_i = M_i(t)$. Given $M_i(t)$, the corresponding nozzle radius, $R(t)$, is determined using the area-Mach number relation for quasi-one-dimensional isentropic flow. Given $R(t)$, $x_s(t)$, then follows from the known nozzle geometry.

Second, given the instantaneous mean separation line position, a single realization of the instantaneous separation line shape, $s(\varphi,t)$, is generated incrementally: at any given angular position $\theta_j = j(2\pi)N^{-1}$, $j=1,2,\ldots,N$, a separation line displacement, $\Delta s_j = s(\varphi_j,t)$, is determined by sampling the cumulative distribution function associated with the displacement amplitude density, Eq. (42).

Third, once N independent displacements, $[\Delta s_1(t), s_2(t), \ldots, \Delta s_N(t)]$, are thus computed, associated instantaneous side-load components, $F_{sy}[H(t)]$ and $F_{sz}[H(t)]$, are calculated via single realization (nonaveraged) versions of Eqs. (43) and (44). [Note: the instantaneous rocket altitude, $H(t)$, is determined via the vertical momentum Eq. (12); this in turn allows determination of the ambient pressure, $P_a[H(t)]$. In addition, the pressure $P_i(t)$ is obtained using the quasi-one-dimensional isentropic relation for P_0/P_i.]

Model simulations were performed using MATLAB/SIMULINK. Single realization time histories of side loading and associated translational and rotational displacements were obtained by numerically integrating the governing equations using a fourth-order Runge Kutta algorithm. Model parameters, given in Table I, are representative of those associated with sounding rockets, e.g., the Peregrine[45–47] and Black Brant.[48] This choice was guided by various scaling arguments, all of which showed that side-load effects on rocket dynamics become increasingly promi-

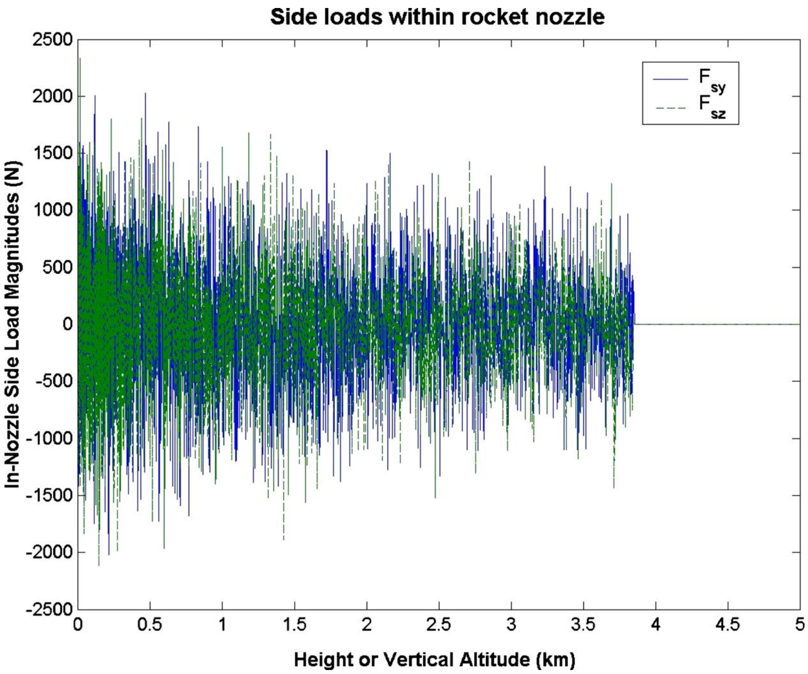

FIG. 5. (Color online) In-nozzle stochastic side loads (n) vs rocket vertical altitude (km).

nent with decreasing rocket size. [The most straightforward of these proceeds as follows: form the ratio of characteristic side-load magnitude to characteristic thrust

$$\frac{F_s}{\rho_e u_e^2 A_e} \sim \frac{(P_a - P_i)2\pi R_e \sigma_s}{k P_e M_e^2 R_e^2} \sim \frac{\sigma_s}{k M_e^2 R_e},$$

where subscripts refer to values at the nozzle exit and where R_e is the nozzle exit radius. Here, we used $P_a \gg P_t$ (where P_i is the characteristic nozzle pressure immediately upstream of the separation-inducing shock), as well as $P_e \sim P_a$ (which is approximately true while the separation-inducing shock lies within the nozzle). Since M_e^2 and σ_s are, in a order of magnitude sense, relatively fixed for a range of rocket nozzle sizes, then it is clear that relative side-load magnitudes increase with decreasing rocket size.]

As soon as rocket ascends from sea-level, an oblique shock system is generated within its exhaust nozzle due to overexpanded flow condition [the isentropic nozzle flow exit pressure being lower than the ambient atmospheric pressure at sea-level, i.e., with NPR $(=P_o/p_a)$ being approximately 70]. Due to adverse pressure gradient and nozzle geometry, flow separation from nozzle walls also occurs just about the same location as the shock. With increasing altitude (i.e., with increasing NPR), the separation line and thus the shock continue to move downstream of the nozzle (as illustrated in Fig. 6). It is to be noted Fig. 6(a) only represents approximate geometry of shock within the nozzle, where the radial [i.e., $R[H(t)]$] and the axial positions [i.e., $x_s[H(t)]$] are related to each other through nozzle geometry, thereby not capturing or emphasizing the detailed structure of complex shock-boundary layer interactions (refer to Ref. 1 for details). The flow within the nozzle continues to be overexpanded till an altitude of approximately 3.85 km. Once the shock exits the nozzle (i.e., at an approximate altitude of 3.85 km), the flow within the nozzle is fully isentropic—any further discrepancy between the nozzle exit pressure and the ambient pressure is compensated through a system of oblique shock diamonds or expansion fans past the nozzle exit plane. Since the nozzle flow is supersonic and fully isentropic past ~4 km altitude, the pressure information past exit plane does not propagate upstream to the nozzle, and hence has no influence on the in-nozzle side loads. So, even though Fig. 7 illustrates that fully isentropic nozzle exit pressure (after ~4 km altitude) is lower than the ambient pressure and continues to be so till an altitude of approximately 30 km, pressure variations due to oblique compression shock diamonds in this zone of the flight (i.e., from ~4 to 30 km) do not affect the in-nozzle stochastic side-load generation process. Thus, side loads are generated within the nozzle as long as the separation line and shock are confined to its interior.

Figure 5 shows a representative time history of both random side-load components, $F_{sy}(t)$ and $F_{sz}(t)$. Several features can be noted. First, it is found that side-load magnitudes are only one to two orders of magnitude smaller than the characteristic thrust; $(F_{sy}, F_{sz}) = O(10^3\ \text{N})$, while thrust computed is of the order of $10^4 - 10^5$ N. Thus, as anticipated (and as will be shown), side loads play a significant role in rocket dynamics. Second, side loading takes place only at low altitudes where ambient pressure remains high enough to force outside air into the nozzle. [The length of the side-load period, T, can be ascertained, e.g., from Fig. 11(b), where it is seen that random forcing of the yaw rate, ω_y, ceases at approximately 11 s.] Third, during the side loading period, a slight decay in side-load magnitudes is apparent. This can be explained by referring to nonaveraged versions of Eqs. (43) and (44) along with Figs. 6 and 7: over $0 \leq t < T$, the pressure difference, $P_i[H(t)] - P_a[H(t)]$, determining the side-load magnitude drops by roughly 39% while the nozzle radius, $R[H(t)]$, increases by only 18%.

A representative set of single realization results, showing time histories for: (i) position of the rocket's center of mass,

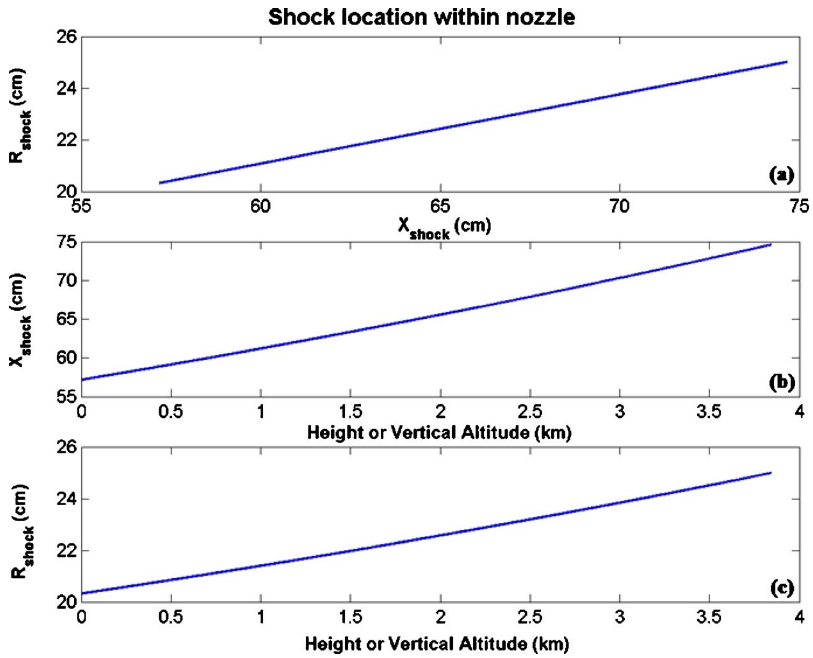

FIG. 6. (Color online) Nozzle shock location (a) radial position of shock (R_{shock} in centimeter) vs its axial position (X_{shock} in centimeter) in the nozzle (note this is only an approximation of the shock structure in a real nozzle and is essentially based on or computed from nozzle geometry), (b) axial position (X_{shock} in centimeter) of shock in nozzle vs rocket vertical altitude from ground (in km), and (c) radial position of shock (R_{shock} in centimeter) vs rocket vertical altitude from ground (in kilometer).

(ii) center of mass translational velocity, and (iii) pitch, yaw and roll rates are presented, respectively, in Figs. 8, 9, and 11. The sets of results shown correspond to a single numerical experiment and in all cases, for purposes of comparison, fully deterministic time histories obtained with random side loads turned off are also included. The initial conditions used in this and all other numerical experiments are as follows: all initial translational and rotational velocities and displacements are zero. Several important observations can be made.

(i) As shown in Fig. 8, random side loads are capable of producing significant (random) lateral displacements, on the order of 1 km over the 25 s simulation period. As also shown, and as expected, no lateral displacement occurs when side loads are suppressed. The magnitudes of observed displacements, in this and all experiments, are of the appropriate scale, i.e., $|F_{s\alpha}|/(\rho_e v_e^2 A_e) \sim M_R \ddot{\eta}/(M_R \ddot{X}_o) \rightarrow \eta(T_f)/X_o(T_f) \sim |F_{s\alpha}|/(\rho_e v_e^2 A_e) = O(10^{-2}-10^{-3})$. Here again, $\eta(t)$ represents either $Y_o(t)$ or $Z_o(t)$ and T_f is the total flight simulation time, i.e., 25 s.

(ii) Due to the same scaling, the effect of side loads on vertical displacements, $X_o(t)$, and thus total displacement, $r_o(t) = \sqrt{X_o^2 + Y_o^2 + Z_o^2}$, is negligible; see Figs. 8(a) and 10.

(iii) The same simple scaling argument can be used to interpret observed rocket velocity histories in Figs. 9(b) and 9(c); here, $\dot{\eta}(T_f)/\dot{X}_o(T_f) |F_{s\alpha}|/(\rho_e v_e^2 A_e)$. Likewise, the scale of the random variation in the vertical velocity component, $\dot{X}_o(t)$, (relative to the no-side-

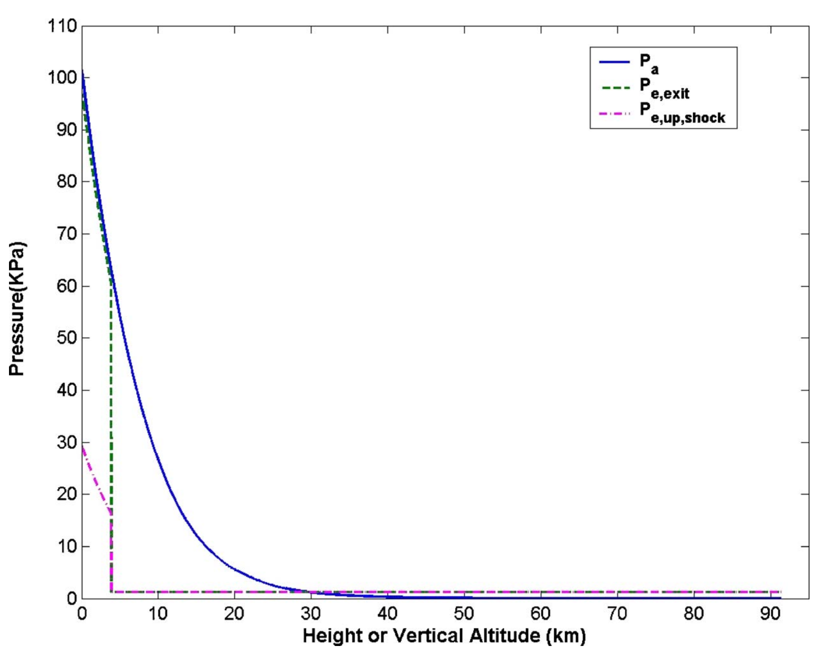

FIG. 7. (Color online) Pressure (in kilopascal) vs altitude above sea-level (in kilometer): p_a is the ambient atmospheric pressure, p_e is the nozzle exit pressure postshock, and $p_{e,up,shock}$ is the pressure upstream of the shock.

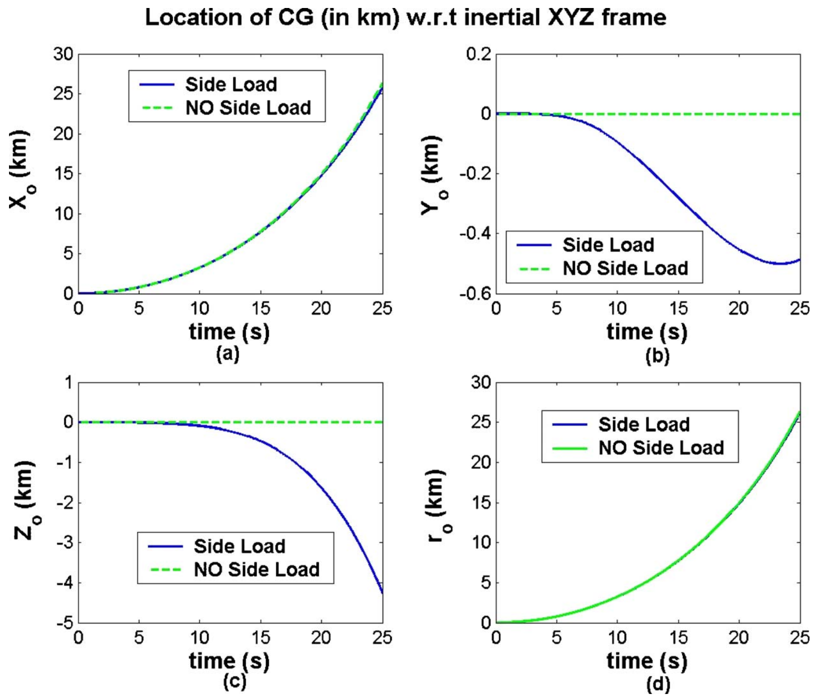

FIG. 8. (Color online) Position time history of the rocket's center of mass O, as measured from an inertial XYZ reference frame (i.e., from ground). (a) Time history of X-position (i.e., vertical height or altitude from ground) of center of mass, (b) time history of Y-position of center of mass, (c) time history of Z-position of center of mass, and (d) time history of radial position (r_o) of center of mass from the origin of inertial XYZ frame, i.e., $r_o=\sqrt{x_o^2+y_o^2+z_o^2}$.

load history) is on the same order [Fig. 9(a)]. Closer inspection of Fig. 9(a), however, yields that the vertical ascent velocity of the rocket is slightly lower when nozzle side loading is taken into account. This could be attributed to transfer of momentum from the longitudinal direction (i.e., x-direction) to lateral directions (i.e., y- and z-directions) as rocket undergoes yaw and pitch under the influence of these stochastic in-nozzle side loads. Qualitatively, the thrust-time curves (equivalently $v_{X,o}$ versus time curves) for similar small, single-stage rockets have been reported to exhibit similar characteristics as shown in Fig. 9(a).[47]

(iv) As expected, and as shown in Figs. 9(b) and 9(c), when side loads are turned off, lateral velocities remain zero throughout any given simulation.

(v) The effect of side loading on total velocity and displacement is small and on the order of $|F_{s\alpha}|/(\rho_e v_e^2 A_e)$; refer to Fig. 10. This simply reflects the dominance of the vertical velocity component relative to the lateral components.

(vi) During the side loading period, pitch and yaw rates exhibit random responses to the random internal torques excited by side loads (refer to Fig. 11); in contrast, and due to the lack of coupling between roll and side loading, the roll rate remains zero throughout the simulated flight given zero initial conditions on roll, pitch and yaw. Following the side-load period, the pitch and yaw rate evolution become wholly deterministic, subject to a random initial condition at $t=T\approx 11$ second (end of side loading period). Under

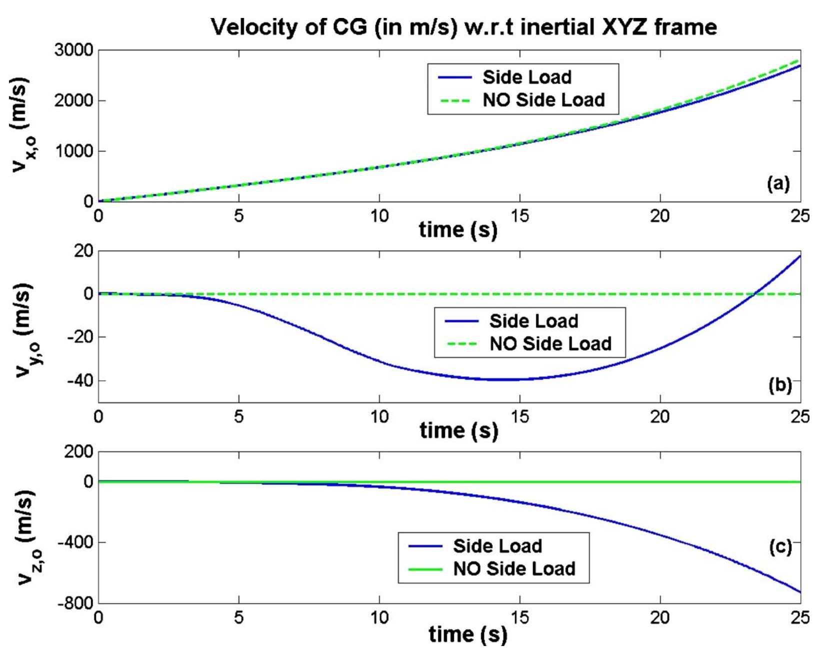

FIG. 9. (Color online) Velocity time history of the rocket's center of mass O, as measured from an inertial XYZ reference frame (i.e., from ground). (a) Time history of velocity of center of mass in X-direction, (b) time history of velocity of center of mass in Y-direction, and (c) time history of velocity of center of mass in Z-direction.

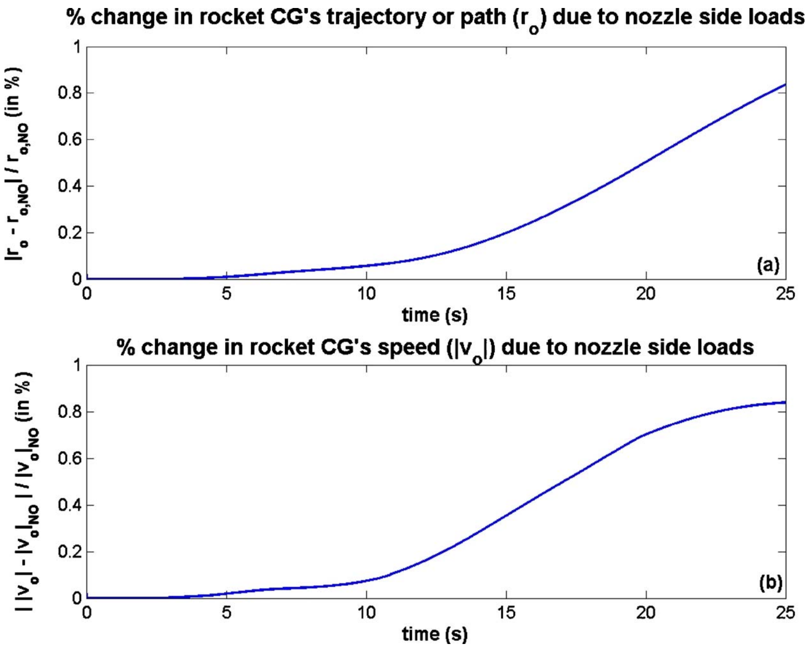

FIG. 10. (Color online) Influence of nozzle side loads on path and speed of rocket during its attitude. (a) percentage change in the path of rocket's center of mass, i.e., $100|r_o - r_{o,\mathrm{NO}}|/r_{o,\mathrm{NO}}\%$ where $r_o = \sqrt{x_o^2 + y_o^2 + z_o^2}$ is the radial position of rocket's center of mass measured from the origin of the inertial XYZ system (b) percentage change in the speed of rocket's center of mass, i.e., $100||v_o| - |v_o|_{\mathrm{NO}}|/|v_o|_{\mathrm{NO}}\%$, where $|v_o| = \sqrt{\dot{x}_o^2 + \dot{y}_o^2 + \dot{z}_o^2}$ is the speed and the subscript "NO" refers to the no side-load scenario.

the no-side-load scenario, since no internal or external torques are present, the rocket rotation remains essentially zero. It is interesting to note from both Figs. 11 and 13 that once the side-loading period is over, the pitch and yaw rotation rates of the rocket tend to move toward the zero mean, thereby emphasizing an underlying rich dynamics associated with a *"mean-reverting"* process. The detailed analyses capturing the nature of this *"mean-reverting"* process will be emphasized in subsequent publications.

The differences in the dynamic response of rigid-body rocket model for side loading and no side load scenarios are thus quite clear from Figs. 8–11. Although the rocket's center-of-mass altitude [i.e., X_o in Fig. 8(a)] and vertical launch velocity [i.e., $v_{X,o}$ in Fig. 9(a)] are not affected much by in-nozzle side loads, it's the rocket lateral motion (i.e., Y_o, Z_o, $v_{Y,o}$, $v_{Z,o}$ in Figs. 8 and 9) that is significantly influenced by these side loads. The rocket during its attitude or ascent thus continues to exhibit deviations (though slight/minor—refer to Fig. 10) from the path that it would have taken had there been no side loads in the nozzle. Also, it is interesting to note that since the side loads in y- and z-directions exhibit nearly same characteristics (or trends), as depicted in Fig. 5, the y- and z-direction motions of the rocket tend to be similar, as could be inferred more clearly from Figs. 13 and 15, thereby implying the stochastic distribution of side loads do not induce any preference in y-direction rocket motion over z-direction motion or vice-versa.

It is clear that Figs. 8–11 only represent a stochastic

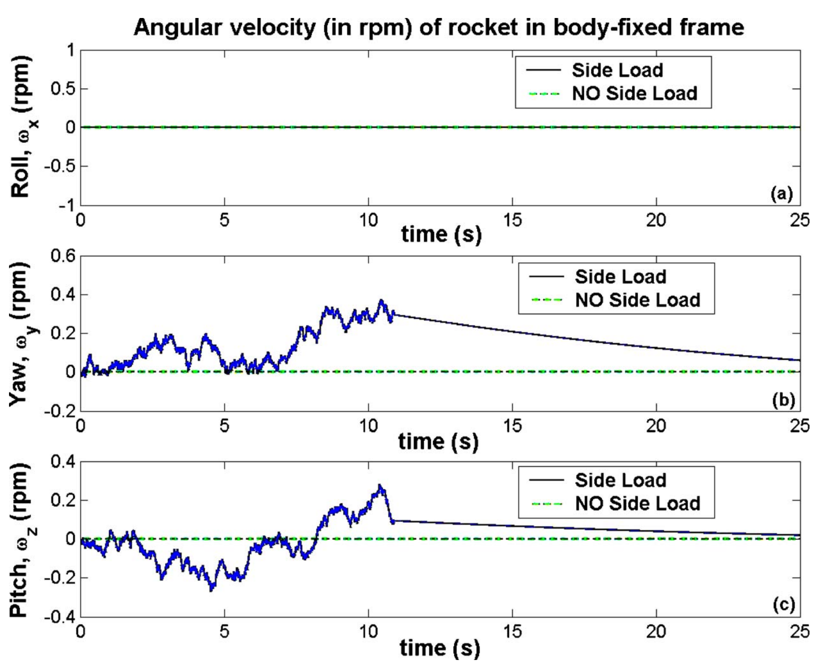

FIG. 11. (Color online) Time history of rocket angular velocity, as measured in body-fixed xyz reference frame attached to center of mass O. (a) Time history of roll angular velocity about x-axis, (b) time history of yaw angular velocity about y *-axis*, and (c) time history of pitch angular velocity about z-axis.

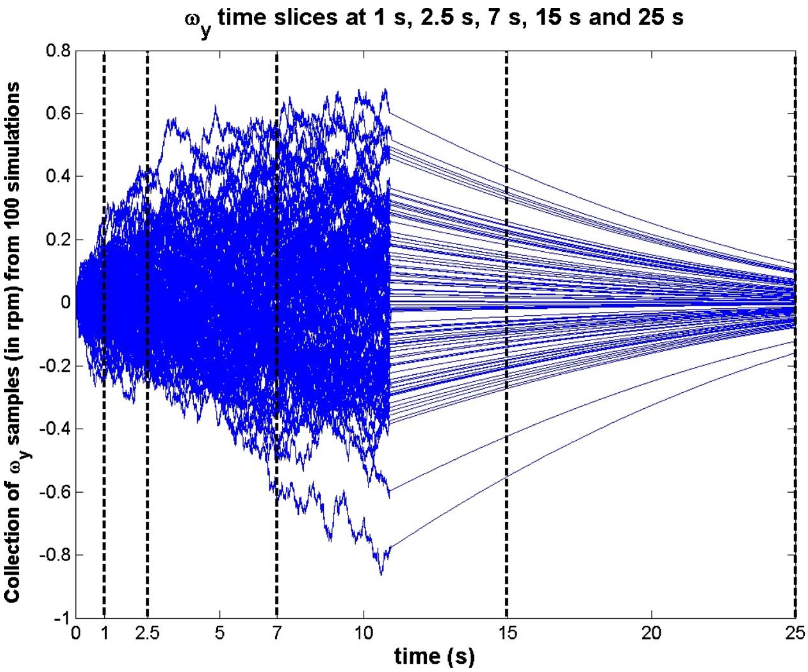

FIG. 12. (Color online) Time histories (i.e., stochastic realizations) of yaw angular velocity, ω_y, of the rocket: complete collection of ω_y samples from 100 simulation runs along with the time slices at 1, 2.5, 7, 15, and 25 s.

sample for the attitude dynamics of rocket. In order to better understand the stochastic effects of side-load generation process on rocket attitude dynamics, numerous (i.e., 100) simulations were performed to get a collection of stochastic samples. Later, several standard tests were performed on these realizations (especially those related to or accounting for the lateral motion of rocket) to capture the underlying stochastic distribution characteristics. Figure 12 shows a collection of time histories (stochastic realizations) of the yaw angular velocity ω_y of rocket obtained from 100 simulations. Knowing this collection of data for yaw angular velocity, it is easy to obtain the mean time history of ω_y as well as the deviations from it (refer to Fig. 13). It could be inferred from Fig. 13 that with increasing (or large) number of stochastic samples, the mean time history of ω_y would correspond to the case of no side loading scenario, however, the error margins or bounds (dependent on the standard deviation, σ) would still be significant. This implies that concluding the average effect of side loads on yaw motion of rocket to be null would be erroneous as deviations from the mean behavior are not insignificant. The variance varies with time—growing steadily as long as shock is within the nozzle and side loads are being generated, and later decaying as shock goes past the exit of nozzle plane (as side loads no longer exist once the shock escapes the nozzle, thereby forcing the rocket to enter a stabilizing state that it would have seen if the side loads were not present at all). Also, Fig. 12 depicts time slices of the collection of ω_y (yaw angular velocity) samples at 1, 2.5, 7, 15, and 25 s. The sample data at these time slices were analyzed to capture the underlying stochas-

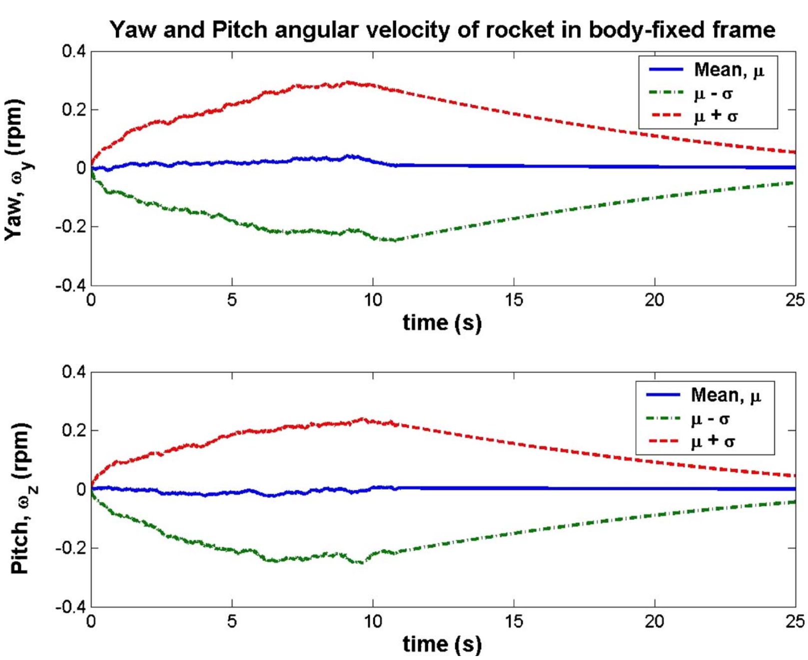

FIG. 13. (Color online) Time history of mean (i.e., μ) yaw angular velocity, ω_y, and pitch angular velocity, ω_z, of the rocket and the errors or deviations [i.e., mean $\pm$ standard deviation (i.e., σ)] based on collection of ω_y and ω_z samples for 100 simulations.

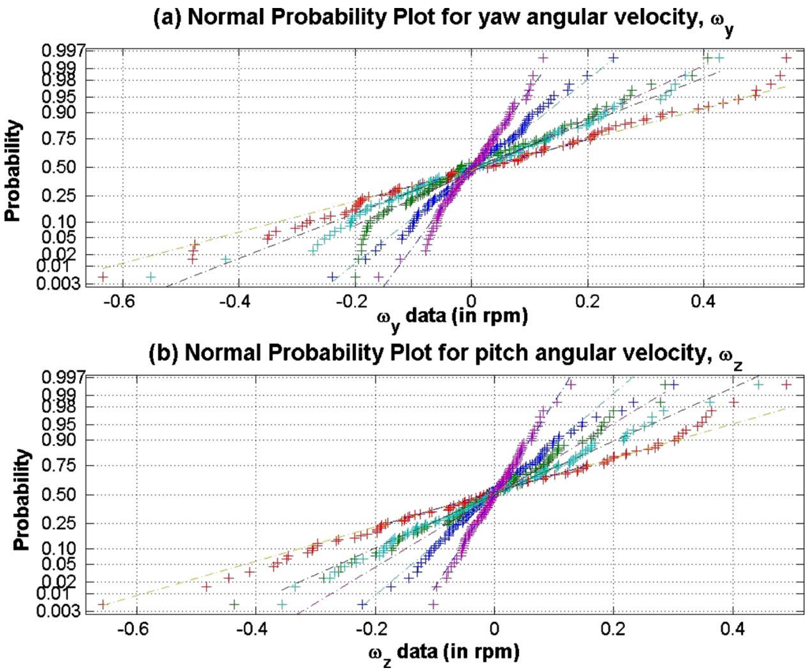

FIG. 14. (Color online) Normal probability plots for the collection data of yaw angular velocity, ω_y, and pitch angular velocity, ω_z, at time slices of 1, 2.5, 7, 15, and 25 s.

tic distribution. Using normal probability plots (refer to Fig. 14) and the Anderson–Darling test it is seen that the underlying probability distributions of yaw angular velocity at every time slice is Gaussian in nature. This is a critical observation as it implies the existence of a unique Chapman–Kolmogorov equation, which once identified/formulated, could be used to analyze the time-evolution of probability distributions of rocket attitude dynamic indices (especially the lateral motion parameters arising from stochastic side loads). Similar observations could be inferred from Figs. 15 and 16. Again, it is clearly evident from Figs. 13 and 15 that side loads do not induce any preference in the y- and z-direction motion parameters, whether they are yaw and pitch angular velocities of the rocket about its center of mass or the lateral translational displacements and velocities of the center of mass.

V. CONCLUSIONS

A long standing, though previously unsolved problem in rocket dynamics, rocket response to random, altitude-dependent nozzle side loads, has been investigated. Numerical experiments, focused on determining single-realization and ensemble average translational and rotational rocket dynamics, incorporate a distributed mass, six-degree of free-

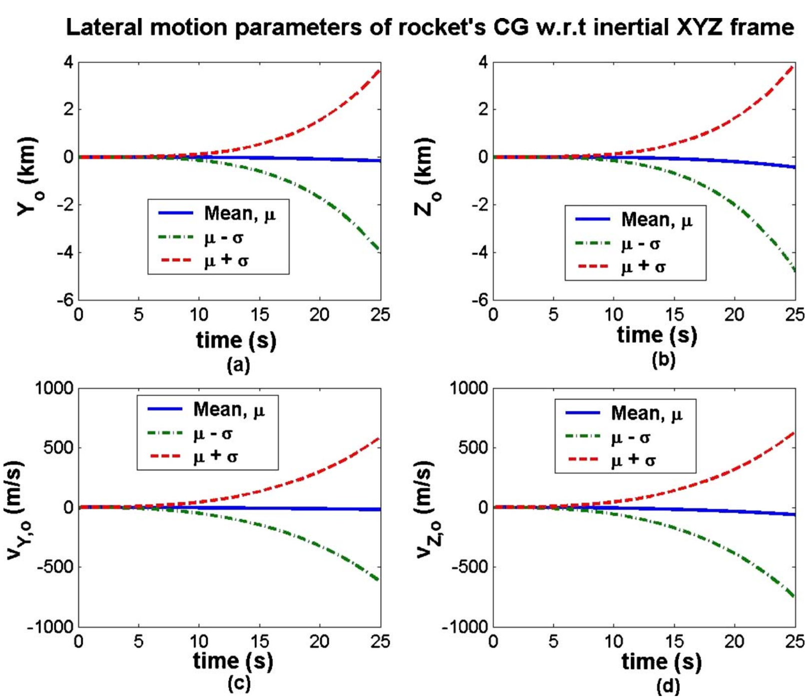

FIG. 15. (Color online) Time history of mean (i.e., μ) lateral motion parameters for the center of mass of the rocket and the corresponding errors or deviations [i.e., mean $\pm$ standard deviation (i.e., σ)] based on the collection of stochastic samples for 100 simulations. (a) Mean path/trajectory for center of mass in the Y-direction along with the deviations, (b) mean path/trajectory for center of mass in the Z-direction along with the deviations, (c) mean velocity of center of mass in the Y-direction along with the deviations, and (d) mean velocity of center of mass in the Z-direction along with the deviations.

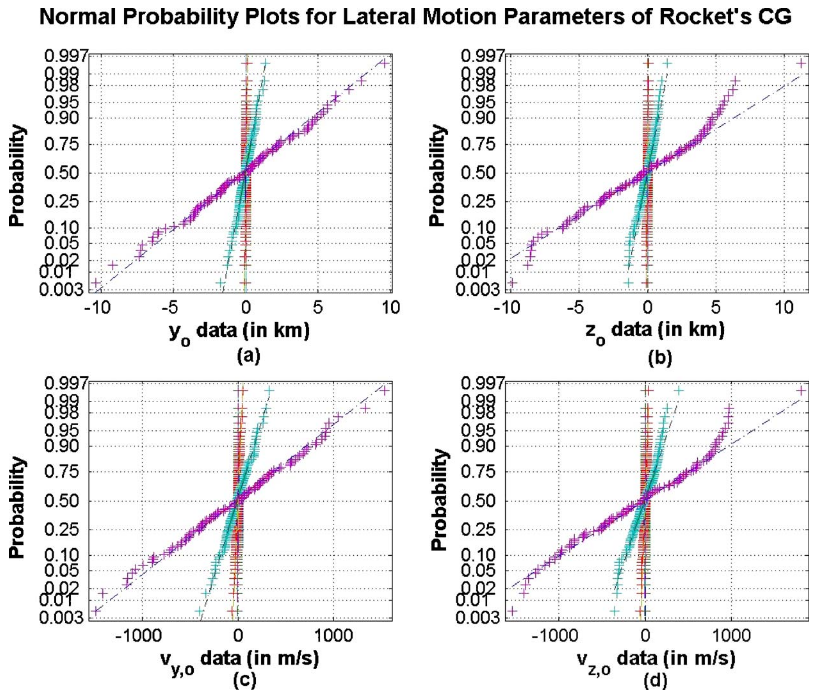

FIG. 16. (Color online) Normal probability plot for the collection data of lateral motion parameters of the rocket's center of mass at time slices of 1, 2.5, 7, 15, and 25 s. (a) Normal probability plot for y_o, (b) normal probability plot for z_o, (c) normal probability plot for $v_{y,o}$ i.e., $\dot{y}_o$, and (d) normal probability plot for $v_{z,o}$ i.e., $\dot{z}_o$.

dom rocket model, representative of small, sounding-rocket-scale rockets. The principal contributions and findings are as follows.

(1) A relatively simple, physically consistent model of random separation-line motion within rigid (nonvibrating) nozzles is developed. By circumventing difficult experimental (or numerical) determination of space-dependent in-nozzle pressure correlations, the proposed model offers distinct advantages over Dumnov's[34] widely used approach. Specifically, in exploiting well-known, nominally universal statistical properties associated with the random motion of shock-separated boundary layers, the model allows analytical determination of altitude-dependent side-load statistics and straightforward Monte Carlo simulation of individual side-load histories.

(2) Scaling indicates that as rocket size decreases, side loads play an increasingly prominent role in rocket dynamics. For example, numerical experiments show that during short (25 s) simulated flight periods, the model rocket can experience random, side-load-driven transverse displacements on the order of several kilometers. Likewise, side loads are found capable of inducing significant random pitch and yaw rates and displacements.

(3) During the low-altitude side-load period (approximately 3.85 km), pitch and yaw rates exhibit rapid increases in stochasticity, as indicated by observed variances; similar behavior is observed for lateral velocities. Following nozzle expulsion of the side-load-inducing shock, however, side-loads cease; nevertheless, subsequent lateral translational dynamics, as well as pitch and yaw rotational dynamics, remain subject to the stochasticity generated during the side-load period. In the case of post-side-load pitch and yaw rate variances, these exhibit a slow decay toward zero. Conversely, lateral translational velocity variances grow at an approximate quadratic rate with altitude.

The implication of the results from this rocket model simulation is clearly twofold: first, rocket attitude-dynamics models not incorporating side loads will predict erroneous launch trajectory and rigid-body rocket motion, which consequently degrades the controller performance owing to greater (often redundant) thrust and attitude control effort and lack of compensation for the stochastic loading on nozzle walls. Subsequent work will include discussion on theoretical stochastic mechanics of a rocket under random side loads, controller design to compensate for undesirable effects of side loads, and development of more enhanced/detailed rocket dynamics model.

[1] J. Östlund and B. Muhammad-Klingmann, Appl. Mech. Rev. **58**, 143 (2005).
[2] H. L. G. Sunley and V. N. Ferriman, J. R. Aeronaut. Soc. **68**, 808 (1964).
[3] M. Summerfield, C. R. Foster, and W. C. Swan, Jet Propul. **24**, 319 (1954).
[4] J. Östlund, T. Damgaard, and M. Frey, J. Propul. Power **20**, 695 (2004).
[5] L. H. Nave and G. A. Coffey, AIAA Pap. **73**, 1284 (1973).
[6] T. Alziary de Roquefort, Proceedings of the Fourth European Symposium on Aerothermodynamics for Space Vehicles, Capua, Italy, 15–18 October, 2001, pp. 93–107.
[7] A. Brown, J. Ruf, D. Reed, M. D'Agostino, and R. Keanini, AIAA Pap. [redacted], 3999 (2002).
[8] J. E. Green, Prog. Aerosp. Sci. **11**, 235 (1970).
[9] A. Zheltovodov, AIAA Pap. **96**, 1977 (1996).
[10] D. Chapman, D. Kuehn, and H. Larson, NACA Report No. 1536, 1958 (unpublished).
[11] E. E. Zukoski, AIAA J. **5**, 1746 (1967).
[12] D. Dolling and M. Murphy, AIAA J. **21**, 1628 (1983).
[13] K. Sinha, K. Mahesh, and G. V. Candler, Phys. Fluids **15**, 2290 (2003).
[14] P. A. Polivanov, A. A. Sidorenko, and A. A. Maslov, AIAA Pap. [redacted], 409 (2009).
[15] F. Onofri and M. Nasuti, AIAA Pap. **99**, 2587 (1999).
[16] T. Shimizu, M. Kodera, and N. Tsuboi, Journal of the Earth Simulator **9**, 19 (2008).
[17] M. Frey and G. Hagemann, AIAA Pap. **99**, 2815. (1999).

[18]M. Frey and G. Hagemann, J. Propul. Power **16**, 478 (2000).
[19]L.-O. Pekkari, AIAA Pap. **94**, 3377 (1994).
[20]R. Schwane and Y. Xia, J. Math. Model. Algorithms **4**, 53 (2005).
[21]E. Lefrançois, Int. J. Numer. Methods Fluids **49**, 349 (2005).
[22]A. J. Calise, N. Melamed, and S. Lee, J. Guid. Control Dyn. **21**, 867 (1998).
[23]G. Dukeman, AIAA Pap. ■, 4559 (2002).
[24]L. Meirovitch, J. Spacecr. Rockets **7**, 186 (1970).
[25]Z. M. Ge and Y. H. Cheng, ASME J. Appl. Mech. **49**, 429 (1982).
[26]A. K. Banerjee, J. Guid. Control Dyn. **23**, 501 (2000).
[27]F. O. Eke and T. C. Mao, Int. J. Mech. Eng. Educ. **30**, 123 (2000).
[28]R. H. Stark, AIAA Pap. ■, 3940 (2005).
[29]R. G. Keanini and A. M. Brown, Eur. J. Mech. B/Fluids **26**, 494 (2007).
[30]C. T. Force, ARS J. **32**, 1095 (1962).
[31]T. Tran and F. O. Eke, Adv. Astronaut. Sci. **119**, 1297 (2004).
[32]Earth Atmosphere Model, NASA Glenn Research Center, URL: http://www.grc.nasa.gov/WWW/K-12/airplane/atmosmet.html [cited 24 February 2010].
[33]R. Schmucker, Technical University of Munich Report Nos. TB-7, -10, -14, 1973 (unpublished).
[34]G. E. Dumnov, AIAA Pap. **96**, 3220 (1996).
[35]S. Deck and A. T. Nguyen, AIAA J. **42**, 1878 (2004).
[36]C. Hagemann, M. Terhardt, M. Frey, P. Reijasse, M. Onofri, F. Nasuti, and J. Östlund, Proceedings of the Fourth International Symposium on Liquid Space Propulsion, German Aerospace Center, Lampoldshausen, Germany, 2000.
[37]G. Settles, I. E. Vas, and S. M. Bogdonoff, AIAA J. **14**, 1709 (1976).
[38]G. Settles, W. Fitzpatrick, and S. Bogdonoff, AIAA J. **17**, 579 (1979).
[39]D. S. Dolling and L. Brusniak, AIAA J. **27**, 734 (1989).
[40]M. E. Erengil, Ph.D. dissertation, University of Texas, 1993.
[41]L. D. Lutes and S. Sarkani, *Stochastic Analysis of Structural and Mechanical Vibrations* (Prentice-Hall, Upper Saddle River, NJ, 1997).
[42]H. W. Liepmann, A. Roshko, and S. Dhawan, NACA Report No. 1100, 1952 (unpublished).
[43]M. E. Erengil and D. S. Dolling, AIAA J. **29**, 1868 (1991).
[44]A. H. Shapiro, *The Dynamics and Thermodynamics of Compressible Fluid Flow*, 1st ed. (Wiley, New York, 1953).
[45]J. Dyer, E. Doran, Z. Dunn, K. Lohner, C. Bayart, A. Sadhwani, G. Zillac, B. Cantwell, and A. Karabeyoglu, AIAA Pap. ■, 5362 (2007).
[46]J. Dyer, G. Zilliac, E. Doran, M. T. Marzoña, K. Lohner, E. Karlik, B. Cantwell, and A. Karabeyoglu, AIAA Pap. ■, 4829 (2008).
[47]Z. Dunn, J. Dyer, K. Lohner, E. Doran, C. Bayart, A. Sadhwani, G. Zilliac, A. Karabeyoglu, and B. Cantwell, AIAA Pap. ■, 5358 (2007).
[48]*Sounding Rocket Program Handbook*, Sounding Rockets Program Office, NASA Goddard Space Flight Center, (Maryland, USA, July 2001).

AUTHOR QUERIES — 140013JAP

#1 Au: Please verify the insertion of the author name “Murphy.”
#2 Au: Please verify the insertion of the author names “Nasuti,” “Hagemann,” and “Xia” in the text.
#3 Au: Please define “CFD.”
#4 Au: Please verify the insertion of the author name “Brown.”
#5 Au: Please verify the changes made in the equation.
#6 Au: Please verify the changes made in the equation.
#7 Au: Please verify the changes made in the equation.
#8 Au: Please verify the renumbering of equation from “21” to “22” as Eq. 21 has been cited above and also verify the subsequent renumbering of equations.
#9 Au: Please verify the insertion of the spelled out form of “NASA.”
#10 Au: Please verify the insertion of Secs. IV and III.
#11 AU: Please verify corrected volume number in Ref. 2.
#12 Au: Please verify the accuracy of the author names in Ref. 4.
#13 Au: Please verify changes made in author names in Ref. 5.
#14 Au: Please provide published information in Ref. 6, if possible.
#15 Au: Please verify the changes made and provide the volume no. in Refs. 7, 14, 23, 28, 45, 46, and 47.
#16 Au: Please verify changes made in author name in Ref. 8.
#17 Au: Please provide published information in Ref. 10, if possible.
#18 Au: Please verify changes made in author names in Ref. 14.
#19 Au: Please verify changes made in author names in Ref. 15.
#20 Au: Please supply the full journal title, the CODEN, and/or ISSN for the journal in Ref. 16.
#21 Au: Please verify changes made in author names in Ref. 17.
#22 Au: Please verify changes made in author names in Ref. 17.
#23 Au: Please supply the full journal title, the CODEN, and/or ISSN for the journal in Ref. 20.
#24 Au: Please verify changes made in author names in Ref.22.
#25 Au: Please verify changes made in author names in Ref.28.
#26 Au: Please supply the full journal title, the CODEN, and/or ISSN for the journal in Ref. 30.
#27 Au: Please provide published information in Ref. 33, if possible.
#28 Au: Please provide date and also published information in Ref. 36, if possible.
#29 Au: Please verify the changes made in year in Ref. 39.
#30 Au: Please provide published information in Ref. 10, if possible.
#31 Au: Please verify changes made in year in Ref. 43.
#32 Au: Please verify changes made in author names in Ref. 44.